Available online at www.sciencedirect.com
ScienceDirect
Journal of volcanology and geothermal research
ELSEVIER
Journal of Volcanology and Geothermal Research 158 (2006) 333–354
www.elsevier.com/locate/jvolgeores

Changing conditions of magma ascent and fragmentation during the Etna 122 BC basaltic Plinian eruption: Evidence from clast microtextures

Julia E. Sable [a,*], Bruce F. Houghton [a,1], Paola Del Carlo [b], Mauro Coltelli [b]

[a] *Department of Geology and Geophysics, SOEST, University of Hawai'i, Honolulu, HI 96822, USA*
[b] *Istituto Nazionale di Geofisica e Vulcanologia, Sezione di Catania, Piazza Roma 2, I-95123 Catania, Italy*

Received 14 December 2005; received in revised form 23 June 2006; accepted 7 July 2006
Available online 20 September 2006

Abstract

The Etna 122 BC basaltic eruption had two Plinian phases, each preceded and followed by weak phreatic and phreatomagmatic activity. This study infers changing eruption dynamics from density, grain size, and microtextural data from the erupted pyroclasts. The Plinian clasts show no evidence for quenching by external water; instead, all clasts are microvesicular and have high bubble number densities relative to the products of weaker basaltic explosive eruptions, suggesting that the 122 BC magma underwent coupled degassing linked to rapid ascent and decompression. This coupled degassing was probably enhanced by crystallization of abundant microlites, which increased the magma's effective viscosity during conduit ascent.

Detailed measurements of vesicles and microlites show wide variations in number densities, size distributions, and shapes among clasts collected over narrow stratigraphic intervals. For such a diversity of clasts to be expelled together, portions of melt with contrasting ascent and degassing histories must have arrived at the fragmentation surface at essentially the same time. We suggest that a parabolic velocity profile across the conduit ensured that magma near the conduit walls ascended more slowly than magma along the axis, leading to a longer residence time and more advanced degrees of outgassing and crystallization in the marginal magma. In our model, accumulation of this outgassed, viscous magma along conduit walls reduced the effective radius of the shallow conduit and led to blockages that ended the Plinian phases.

Keywords: basaltic Plinian; Etna; vesicles; microlites; conduit dynamics

1. Introduction

1.1. Etna's explosive history

The 122 BC eruption of Etna is one of only four well-documented examples of basaltic Plinian volcanism worldwide (Williams, 1983; Walker et al., 1984; Coltelli et al., 1998). This study uses multiple techniques to understand the mechanisms and conditions that allowed basaltic magma to erupt with such high intensity. Powerful explosive eruptions are significant in the Quaternary record at Etna (Coltelli et al., 2000). Etna's eruptive history since 1500 BC includes eleven eruptions with subplinian phases and one Plinian event (Branca and Del Carlo, 2004). Our work will contribute to efforts to predict and prepare for the hazards

* Corresponding author. Present address: P.O. Box 5039, Bozeman, MT 59717, USA. Tel.: +1 808 956 8558; fax: +1 808 956 5512.
E-mail address: jesable@soest.hawaii.edu (J.E. Sable).

0377-0273/$ - see front matter © 2006 Elsevier B.V. All rights reserved.
doi:10.1016/j.jvolgeores.2006.07.006

associated with future intense explosive eruptions at Etna and other basaltic volcanoes.

1.2. Basaltic explosive mechanisms

Like many basaltic volcanoes (Simkin and Siebert, 1994), Etna typically erupts in effusive to weakly explosive styles (Chester et al., 1985; Branca and Del Carlo, 2004; Taddeucci et al., 2005). The ascent of basaltic magma at volcanoes such as Etna, Stromboli, and Kilauea is generally believed to involve decoupled degassing, in which bubbles are able to migrate upward within relatively slowly ascending melt (Blackburn et al., 1976; Wilson and Head, 1981; Vergniolle and Jaupart, 1986; Head and Wilson, 1989; Jaupart and Vergniolle, 1989; Parfitt and Wilson, 1995; Seyfried and Freundt, 2000). In contrast, coupled degassing refers to the situation typical of more silicic melts where bubbles are immobile relative to the melt (Wilson et al., 1980; Papale et al., 1998). The intensity of basaltic explosive behavior is strongly determined by the extent of decoupling of gas from melt, which is, in turn, a function of the relative rates of ascent of melt and bubbles and the extent of bubble coalescence (e.g., Jaupart, 1998; Papale et al., 1998; Denlinger and Hoblitt, 1999; Parfitt, 2004).

Hawaiian fountaining eruptions are associated with a high magma ascent rate and a relatively low degree of bubble coalescence, leading to partially coupled behavior in the shallow conduit and producing a population of mm to cm scale bubbles (Vergniolle and Jaupart, 1986; Parfitt and Wilson, 1995). Strombolian explosions occur at lower melt ascent rates, at which gas slugs can form either by dynamic coalescence in the conduit (Parfitt and Wilson, 1995) or by collapse of a static foam in the magma chamber (Vergniolle and Jaupart, 1986; Vergniolle, 1996). The large (≥ 1 m) gas slugs decouple from and ascend freely through the melt, triggering discrete explosions at the free surface.

The majority of Etna's eruptions fit the above models, but the Plinian eruption of 122 BC and several subplinian events are not compatible with either model due to their higher intensities and sustained eruption styles. Coupled degassing is required for magma to accelerate to the velocity necessary to produce a Plinian explosion (Jaupart and Allegre, 1991). In such a scenario, bubble nucleation is initially delayed by kinetic barriers (e.g., Lyakhovsky et al., 1996), volatile supersaturation develops in the melt, and finally bubbles nucleate in a runaway fashion accompanied by major acceleration that may drive the melt through the glass transition (Papale, 1999). Coupled degassing is most readily achieved when the melt is highly viscous, as is common for high-silica melts (Sparks et al., 1994; Cashman et al., 2000).

A mechanism to suppress or delay decoupled degassing behavior and promote physical coupling between gas and melt in basaltic magma seems essential to permit Plinian eruptions of magma of this composition. The basaltic magma may be forced to adopt coupled behavior either by an increase in effective viscosity, or by vesiculation over a time span too short to permit bubbles to decouple fully from the melt. Three mechanisms that may act in isolation or in combination are: (1) very rapid ascent producing a delayed and shallow onset of degassing; (2) instantaneous decompression accompanying unloading due to caldera development or flank instability (Coltelli et al., 1998); and (3) microlite crystallization inducing rheological change.

1.3. Previous work

According to Coltelli et al.'s (1998) map of the 122 BC fall deposit (Fig. 1), the area within the 10 cm isopach is 530 km^2, confirming that this deposit is Plinian by Walker's (1973) classification. This is consistent with Roman chronicles that describe a large eruption with an ash cloud that hid the sun for days. The inferred vent is near Etna's summit, now buried under the modern summit cone, and the dispersal axis is to the southeast. The total volume of the eruption is 0.4 km^3 DRE (Coltelli et al., 1998). The calculated column height is 24–26 km with an estimated average mass eruption rate of $5.0–8.5 \times 10^7$ kg s^{-1} (Carey and Sparks, 1986; Coltelli et al., 1998).

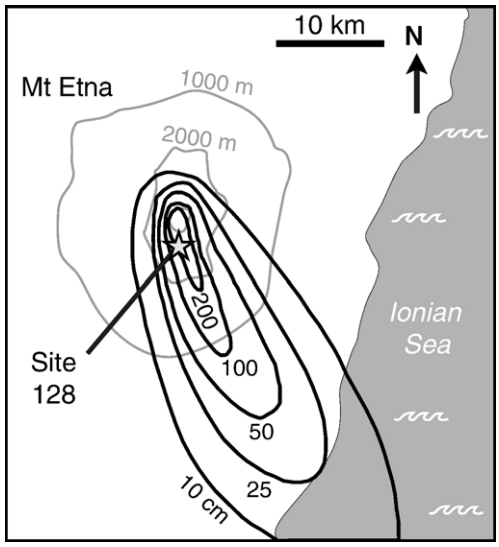

Fig. 1. Isopach map of the Etna 122 BC Plinian fall after Coltelli et al. (1998). Topographic contours (gray) are in meters, isopachs (black) are in centimeters. Star indicates Site 128, the principal sample site.

Coltelli et al. (1998) divide the 122 BC deposit into seven units, A–G (Table 1). Unit A is a thin layer of well-sorted, coarse black ash of Strombolian dispersal. Units C and E are made up of well-sorted scoria and subordinate wall rock lithic lapilli, and are interpreted as Plinian falls. Units B, D, F, and G are tuffs ranging from bedded to massive in character, attributed to phreatomagmatic and phreatic phases of activity. Thus the 122 BC eruption had two Plinian phases, each preceded and followed by periods of weaker phreatomagmatic activity. Coltelli et al. (1998) also give analyses of bulk chemistry for each Plinian unit.

Coltelli et al. (1998) propose an eruption model in which a sudden decompression event triggered runaway bubble nucleation in the 122 BC melt, allowing the magma to develop rapidly into a microvesicular foam. One possible cause of such a decompression is unloading by a collapse, but there is no evidence for contemporaneous slope failure, and caldera collapse was unlikely at the beginning of the eruption sequence. Instead, the authors suggest a model in which the rapid injection of >1 km^3 of buoyant magma into the volcanic edifice caused abrupt elastic deformation of the eastern flank.

Table 1
Proximal stratigraphy for the 122 BC eruption of Etna

Unit	Max thickness (cm)	Wall rock (wt %)	Description	Interpretation
G	220	<10	Massive fine tuff with large accretionary lapilli	Late phreatic explosions
F	54	<5	Vesiculated coarse and fine brown tuff	Final phreatomagmatic phase with minor surge component
E	51	7–12	Well sorted normal graded lapilli fall	Second Plinian magmatic phase
D	37	<10	Indurated, bedded and vesiculated, poorly sorted, fine tuff	Phreatomagmatic phase dividing Plinian phases
C	169	10–26	Well sorted lapilli fall	First Plinian magmatic phase
B	17	<10	Yellowish fine lithic-rich poorly sorted, tuff	Weak phreatomagmatic phase
A	11	–	Well-sorted coarse juvenile ash	Strombolian initial phase

Thicknesses, unit descriptions, and interpretations are summarized in Coltelli et al. (1998). Wall rock contents were measured for this study.

Del Carlo and Pompilio (2004) report detailed chemical analyses of glass, crystals, and melt inclusions in clasts from Plinian units C and E as well as in other Etna magmas. Electron microprobe analyses show that the composition of matrix glass is hawaiite while melt inclusions are mugearite (i.e., higher in SiO_2 and alkalis). Pre-eruptive volatile contents were measured by transmission IR spectroscopy in melt inclusions within olivine phenocrysts, yielding $1.0–3.1 \pm 0.1$ wt.% H_2O and $200–900 \pm 100$ ppm CO_2. In the 122 BC clasts, volatile contents vary widely with weak or no dependence on the overall composition of the melt inclusions, whereas in other Etna magmas, variations in volatile content correlate with variations in other incompatible elements. The authors suggest that cooling, crystallization, and differentiation were relatively limited in the 122 BC magma, and the magma probably ascended rapidly with respect to other eruptions at Etna. Using the solubility model of Dixon and Stolper (1995), they estimate that the melt inclusions were trapped at a minimum pressure in the range of 50 to 210 MPa.

Houghton et al. (2004a) interpret some aspects of the eruption's evolution with time based on measurements of grain size and clast densities/vesicularities. The authors suggest that trends toward lower vesicularities late in the first Plinian phase and throughout the second Plinian phase indicate considerable cross-conduit heterogeneity in the magma. In their model, slower-moving magma along the walls of the conduit had more opportunity for outgassing and crystallization, leading to increased viscosity, which further reduced the ascent velocity of this marginal magma. Buildup of slow or stagnant magma along the margins reduced the effective conduit radius and ultimately caused discharge to wane. The current study adds detail and expands on this conduit model using additional macroscopic data as well as qualitative and quantitative characterization of clast microtextures.

1.4. Questions

Three main questions are addressed in this paper. First, what processes caused the basaltic magma to erupt in Plinian fashion? Second, how did the degassing behavior of the 122 BC magma change with time? Third, why did the Plinian plume subside and terminate twice, with phreatomagmatic episodes of significantly weaker intensity intervening? We address these questions via quantitative studies of textural diversity in the pyroclasts from multiple stratigraphic levels in the Plinian units of the deposit.

2. Methods

The principal sample site for this study, Site 128 (Fig. 1), is the most proximal exposure along the dispersal axis of the 122 BC deposits. Eleven pairs of samples were collected from stratigraphic zones 5–10 cm thick. Each pair includes one sample for grain size and one for microtextural studies. Grain size and componentry were measured in the laboratory at 1/2ϕ intervals. For the microtextural samples, consisting of 100 clasts in the 16–32 mm diameter range, clast morphology and surface texture were described and classified. Distributions of clast densities were measured and interpreted following the methods of several other studies (e.g., Sparks and Brazier, 1982; Houghton and Wilson, 1989; Cashman and Mangan, 1994; Klug and Cashman, 1994). The density distribution of each sample was used to select a smaller subset of 4–8 clasts including representative examples of maximum, minimum, and modal vesicularities. These subsets of clasts were made into polished thin sections for detailed quantitative textural measurements.

Microscopic vesicle textures were quantified in 17 representative clasts selected based on stratigraphic position and clast density. Sets of nested images were acquired at four magnifications. The lowest magnification was captured using an HP flatbed scanner, and the three higher magnifications were imaged on a JEOL-5900LV scanning electron microscope (SEM) with 20 kV accelerating voltage and 1 nA beam current. The resolutions of the digital images from lowest to highest magnification were 47.2, 252, 1000, and 2520 pixels/mm. Images were edited for contrast and clarity in Adobe Photoshop, and bubble areas were measured in Scion Image.

The use of two-dimensional images to represent three-dimensional distributions of vesicles and crystals presents a challenge as discussed by Mangan et al. (1993). Corrections were applied using the stereological technique of Sahagian and Proussevitch (1998). The stereological conversion assumes that vesicles are spherical. This is not the case for the 122 BC samples, but no applicable methods exist for irregular bubble shapes. The bubble sizes indicated in the tables and figures are the diameters and radii of equivalent spheres calculated in the 2D to 3D conversion.

Microlites were also studied qualitatively and quantitatively. Separate sets of SEM images were acquired at high magnification (25,200 pixels/mm) to resolve the microlites. Number density, volume abundance, characteristic size, and habit of each mineral phase were observed and/or measured.

3. Results

3.1. Eruption dispersal

The deposits of Plinian phases C and E extend beyond 30 km from vent (Fig. 1; Coltelli et al., 1998). The dispersal trends of units C and E can be compared using profiles along the dispersal axis (Fig. 2) after Pyle (1989). Both units are sheet-forming and have similar $t_{1/2}$ (linear thickness half-distance; Houghton et al., 2004b) values of 10.3 km (unit C) and 10.2 km (unit E), indicating that the two phases were similar in intensity. The smaller volume of tephra in unit E implies a shorter duration for the second Plinian phase.

3.2. Grain size, componentry, and clast morphology

Median grain size and componentry data were first presented in Houghton et al. (2004a) with some tentative interpretations. In the current study, sorting data are added and the overall dataset is interpreted in more detail. The median grain size at the principal sample site is consistently relatively coarse (between −2 and −4ϕ) but shows minor fluctuations with time, some abrupt and others gradational (Fig. 3). The largest juvenile clasts are found in sample C6, which we infer to represent the peak intensity of the Plinian eruption. Sorting varies throughout the units. The samples with the coarsest median grain size (C2 and C6) show good ($\sigma\phi \approx 1.0$) sorting, while finer-grained samples are more poorly sorted, such as C7, C4, and E3. The grain size characteristics of the Etna 122 BC samples are identical to those of silicic Plinian falls (Walker, 1980, 1981) and very different from archetypical phreatoplinian falls

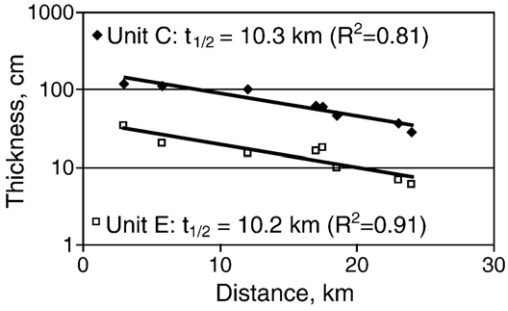

Fig. 2. Plot of thickness vs. linear distance from vent for Plinian units C and E of the Etna 122 BC deposit, with thickness on a logarithmic scale (P. Del Carlo and M. Coltelli, unpublished data). Measurements were taken close to or on the axis of dispersal. The calculated linear thickness half distances ($t_{1/2}$) values are 10.3 km for unit C and 10.2 km for unit E. Quality of fit is indicated by R^2 values.

(Self and Sparks, 1978; Walker, 1981). Wall rock content generally increases with increasing median grain size throughout the sequence. At the tops of units C and E, the lithic content decreases along with the grain size (Fig. 3).

The 122 BC juvenile clasts do not exhibit quench textures or breadcrust cracks. The clasts are also conspicuously lacking in highly fluid achneliths, Pele's tears, fusiform bombs, and other features associated with Hawaiian and Strombolian basaltic deposits (Richter et al., 1970; Swanson et al., 1979). Instead, samples are typically dominated by blocky, ragged, and cauliflower-like forms. Curviplanar clasts, with flat or concave surfaces bounded by angular edges, are rare in all samples except E3, which contains 25% such clasts.

3.3. Clast density and vesicularity

We have revisited and supplemented the density data of Houghton et al. (2004a) as the foundation for selecting clasts for microtextural analysis. Distributions of Etna 122 BC clast densities, and thus clast vesicularities, show that the clast population from the opening of Plinian phase C included a significant

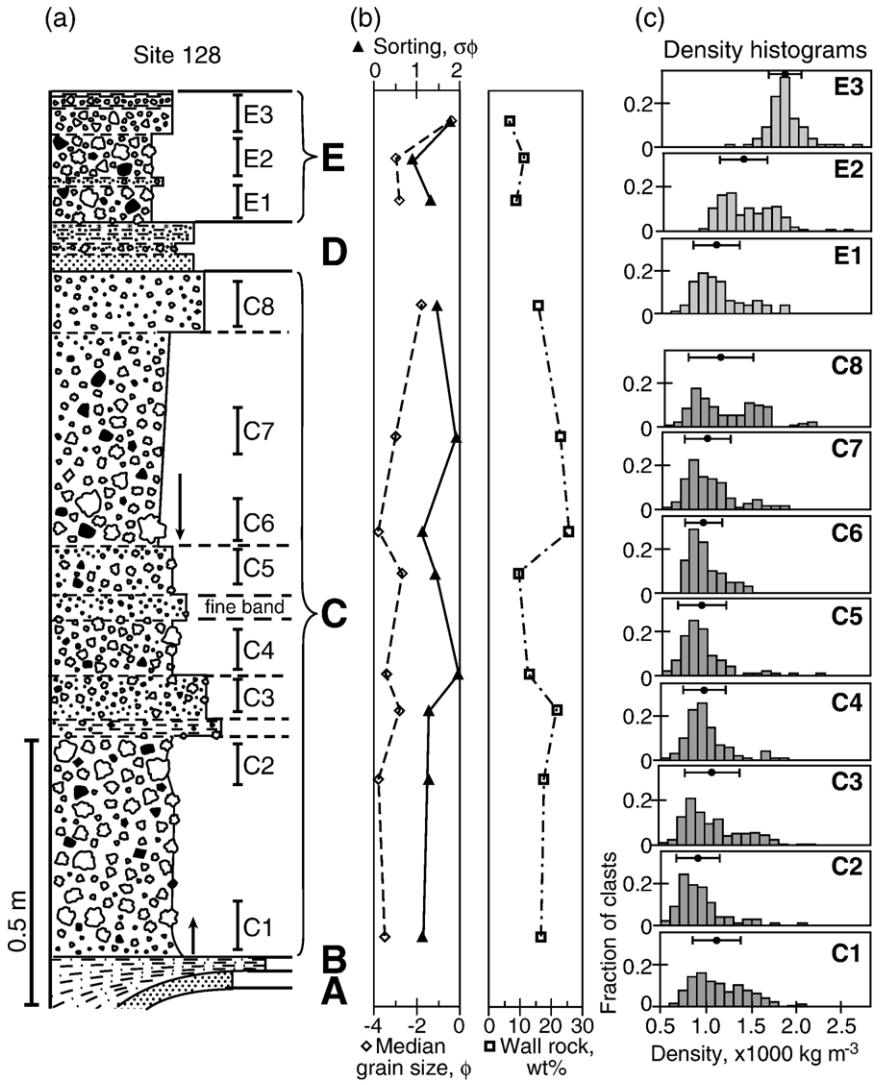

Fig. 3. (a) Stratigraphic column of proximal Site 128 with sample intervals labeled. Vertical arrows indicate graded intervals and point in direction of coarsening. (b) Median grain size, sorting, and wall rock content are plotted for each sample. (c) Histograms of clast density for samples of 100 clasts in the 16–32 mm diameter range. Dots above histograms mark mean densities, and bars extend 1 standard deviation to each side. All samples have positive skewness (high density tails on the distributions).

proportion of high-density clasts (Fig. 3). As the eruption intensity increased, the clast population became more uniform but still had a small proportion of high-density clasts. The proportion of dense clasts then increased until a bimodal density distribution developed near the end of phase C (sample C8), coincident with a decrease in grain size. The secondary peak in the bimodal distribution of C8 matches the dense tails in earlier samples C2 through C7 (1500 to 1700 kg m^{-3}). For unit E, the density distribution broadens early (sample E2) and then forms a single distinct peak (sample E3) of high-density clasts.

3.4. Vesicle data

3.4.1. Qualitative observations

The 122 BC clasts have high bubble number densities, with respect to Hawaiian and Strombolian ejecta, and a wide range of bubble textures (Fig. 4). All samples are microvesicular, with bubbles sizes ranging from 5 μm to 5 mm in diameter. Very small (<10 μm) bubbles are rare. The most crystalline clasts contain tiny, angular voids between microlites (Fig. 4d), but these "dikty-taxitic" textures result from contraction during microlite crystallization, not vesiculation (Walker, 1989; Saar and Manga, 1999; J. E. Hammer personal communication,

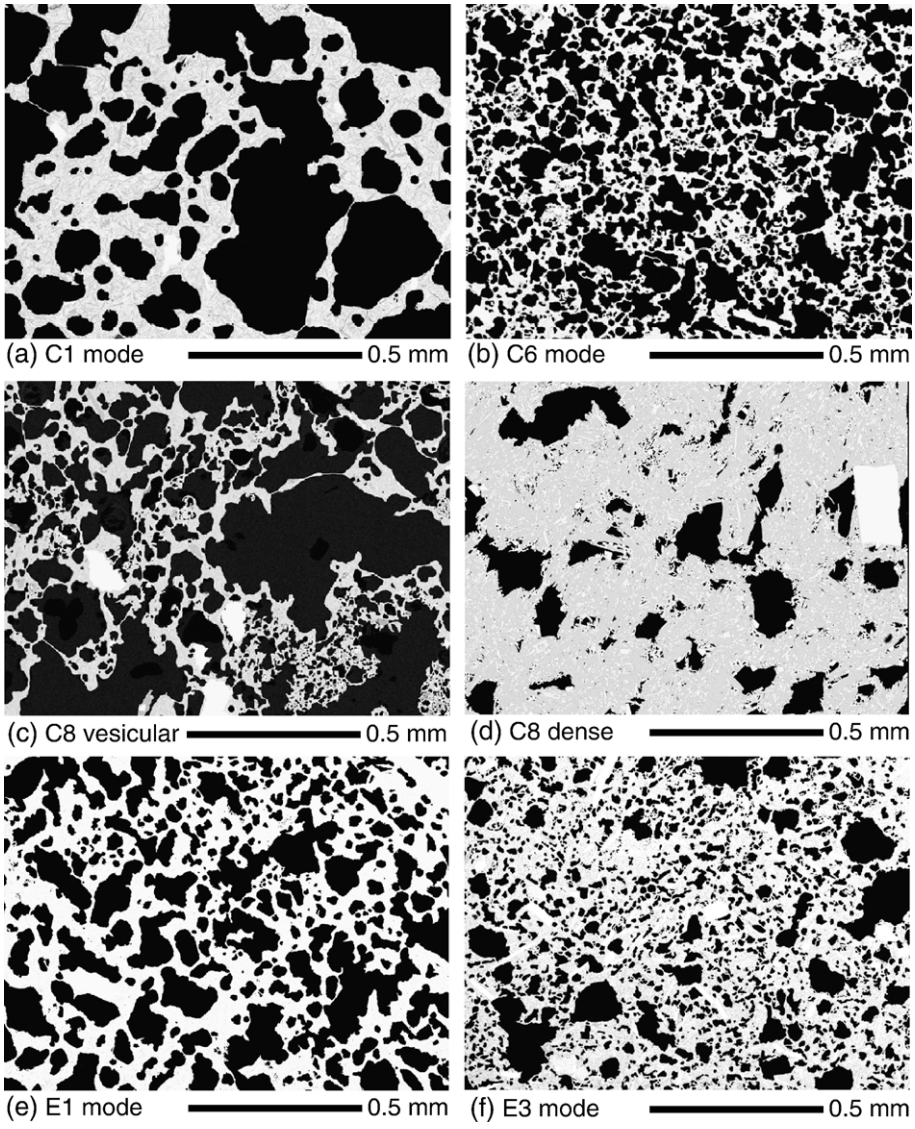

Fig. 4. Selected SEM images of vesicle textures. Bubbles are black; glass and crystals are pale grey to white.

2005). Most bubbles are surrounded by melt, but a few bubbles adhere to phenocrysts. In general, bubbles are uniformly dispersed in the 122 BC clasts regardless of size, but some clasts also have irregular zones 0.2–0.5 mm wide that are dominated by intermediate or small vesicles (e.g. Fig. 4c).

Complex shapes characterize all bubbles larger than 50 μm as well as most bubbles down to 10 μm diameter. Some bubbles have shapes composed of merged convex rounded forms (e.g. Fig. 4a), while others have shapes that are more attenuated with some concave margins (e.g. Fig. 4d). No preferred direction of elongation is observed.

3.4.2. Quantitative measurements

As previously described, 3–4 thin sections of mode, minimum, and maximum density clasts were selected from each 100-clast sample for quantitative measurements of vesicle size and number density. The modal clast of a sample is assumed to be representative of the bulk of the magma erupted at a given time, and the low and high density clasts constrain the degree of heterogeneity at that time.

Total bubble number densities for the Etna 122 BC clasts range from 3×10^6 cm^{-3} to 9×10^7 cm^{-3} (Table 2; Fig. 5). These values partially overlap those measured in silicic Plinian pumice (6×10^7 to 1×10^{10} cm^{-3}; Klug

Table 2
Bubble size ranges, typical sizes, and total number densities (N_{Vtot}) for explosive products of a range of compositions

Eruption	Sample	Diameter range (cm)	Typical diameter (cm)	N_{Vtot} (cm^{-3}, bulk rock)
Etna 122 BC[a]	Early C mode	0.0007–0.25	0.0501	2.57×10^6
	Peak C mode	0.0007–0.25	0.0237	3.42×10^7
	Late C mode	0.0007–0.158	0.0199	1.71×10^7
	Early E mode	0.0007–0.316	0.0398	8.07×10^6
	Mid E mode	0.0007–0.199	0.0100	2.83×10^7
	Late E mode	0.0007–0.158	0.0158	6.13×10^7
Keanakako'i[b]	520b			5.61×10^6
	517b			1.32×10^6
	508f			1.48×10^6
	502h			1.71×10^6
	409b			1.44×10^6
Kilauea reticulite[c]	2500R1	0.001–0.2	0.107	1.78×10^3
	45-2	0.001–0.36	0.182	3.75×10^2
	45-3	0.001–0.36	0.184	3.32×10^2
	2500R4-A	0.001–0.46	0.228	1.10×10^2
Kilauea scoria[c]	487T	0.001–0.12	0.009	1.77×10^5
	500S1	0.001–0.12	0.009	1.60×10^5
	OoB	0.001–0.14	0.012	1.10×10^5
	282T	0.001–0.18	0.011	7.30×10^4
	300T2	0.001–0.10	0.010	1.20×10^5
Stromboli[d]	1952 – high			5.39×10^4
	1911 – low			3.44×10^5
Vesuvius[e]	EU2 – mean	0.0008–0.267	0.005	5.6×10^8
	EU3b – mean2	0.0008–0.435	0.005	8.1×10^7
	EU3t – mean2	0.0005–0.413	0.002	8.8×10^8
	EU4 – mean2	0.0008–0.248	0.002	5.2×10^8
Campanian Ignimbrite[f]	CI60 – 70m1	0.0011–0.0016	0.0011	1.4×10^8
	CI60 – 70t	0.0011–0.0016	0.0016	8.2×10^7
	CI110 – 120m1	0.0012–0.0013	0.0012	1.3×10^8
	CI110 – 120t	0.0012–0.0013	0.0013	1.3×10^8
Mount St Helens[g]	Gray	0.0002–0.3	0.002	2.0×10^9
	White	0.0002–0.3	0.005	8.2×10^8
Mazama 7700 BP[h]	PF15	0.0002–0.5	0.002	7.76×10^9
	WT9	0.0002–0.4	0.001	1.00×10^{10}
	CP10	0.0002–0.6	0.005	2.29×10^9
	CP11	0.0002–0.2	0.004	1.29×10^9
	CP14	0.0002–0.8	0.501	7.76×10^7

Minimum bubble diameters are estimates that depend on limiting image resolution. Total bubble number densities are per volume of bulk rock, rather than per volume of melt.
References: [a]This study, [b]Mastin et al. (2004); [c]Mangan and Cashman, (1996); [d]Lautze and Houghton (2005); [e]Gurioli et al. (2005); [f]Polacci et al. (2003); [g]Klug and Cashman (1994); [h]Klug et al. (2002).

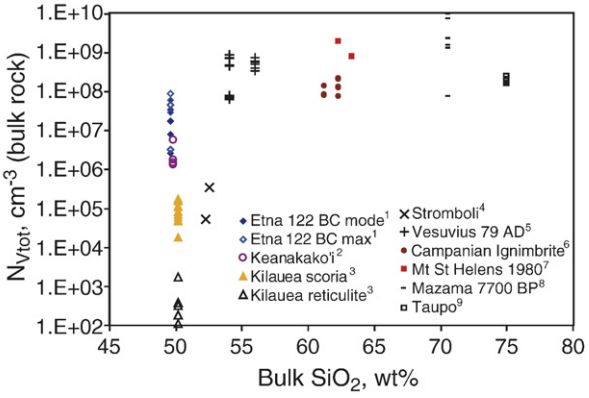

Fig. 5. Comparison of total bubble number densities (N_{Vtot}) for explosive eruptions with a range of magma compositions indicated by bulk SiO_2 content. Number densities are given per volume of bulk rock, rather than per volume of melt. References: (1) This study; (2) Garcia et al. (2003), Mastin et al. (2004); (3) Garcia et al. (1992), Mangan and Cashman (1996); (4) Lautze and Houghton (2005); (5) Civetta et al. (1991), Gurioli et al. (2005); (6) Signorelli et al. (1999), Polacci et al. (2003); (7) Criswell (1987), Klug and Cashman (1994); (8) Klug et al. (2002); (9) Froggatt (1981), B. Houghton, unpublished data.

and Cashman, 1994; Klug et al., 2002; Gurioli et al., 2005). Typical basaltic scoria and reticulite have lower bubble number densities, ranging between 1×10^2 and 4×10^5 cm^{-3} (Mangan and Cashman, 1996, Lautze and Houghton, 2005). The only well-characterized basaltic pyroclasts with bubble number densities comparable to those of Etna 122 BC come from a subunit of the Keanakako'i Ash of Kilauea, which, although phreatomagmatic, probably was of subplinian intensity (Mastin et al., 2004).

The range of bubble sizes in the Etna 122 BC clasts covers three orders of magnitude (Fig. 5), while the widest bubble size range in typical cone-forming basaltic tephra spans only two and lacks the smallest bubbles (Table 2; Mangan and Cashman, 1996; Lautze and Houghton, 2005). In comparison to silicic pumice, the 122 BC clasts have a similar range of bubble sizes but a coarser mode bubble diameter (Table 2).

Distributions of vesicle sizes are shown as histograms of volume fraction vesicles versus vesicle diameter (Fig. 6). The modal density clast from sample C1 has a narrower but coarser bubble size peak than the other modal clasts of unit C. The distribution of bubble sizes shifts toward smaller values in samples C2 and C6, but includes significant subpopulations of both coarser and finer vesicles by the end of phase C (sample C8). The modal density clast from the start of phase E (sample E1) has a coarse bubble size peak similar to the start of phase C. Overall vesicularity then decreases (sample E2) until vesicles of all sizes are strongly depleted in sample E3. All minimum density clasts from phases C and E are rich in large vesicles. The maximum density clasts at the start and end of phase C (samples C1 and C8) also have modes of coarse vesicle sizes, but the dense clasts in phase E have smaller bubbles (samples E1 and E2) or a lower overall volume fraction vesicles (sample E3).

3.5. Crystal data

3.5.1. Phenocrysts

Phenocrysts make up 1–10% of the samples by volume (Coltelli et al., 1998), and include plagioclase and minor clinopyroxene, olivine, and iron–titanium oxide. Plagioclase phenocrysts are subhedral and commonly show zoning and some resorption textures. Clinopyroxene phenocrysts are euhedral to rounded. Fe–Ti oxide phenocrysts are equant and subangular. Although phenocrysts provide information about conduit processes for some eruptions (e.g., Rutherford and Hill, 1993), this is not the case for the Etna 122 BC phenocrysts. It is difficult to distinguish features related to conduit ascent from features inherited from the phenocrysts' formation in the magma storage zone. Thus we reserve our detailed study for the microlites, which indicate conduit processes more directly.

3.5.2. Microlite observations

Clasts in silicic Plinian deposits are typically poor in microlites (Hildreth, 1983; Fierstein and Hildreth, 1992; Sutton, 1995), and Hawaiian–Strombolian ejecta also have very low to moderate microlite contents (e.g., Lautze and Houghton, 2005; Polacci et al., 2006). In contrast, microlites are abundant in samples from all stratigraphic levels of the Etna 122 BC deposits. The groundmass textures of 25 clasts have been characterized qualitatively and quantitatively. Sizes and habits of the microlites are extremely diverse (Fig. 7; Table 3). We group the textures into three categories (holocrystalline, hypocrystalline, hypohyaline) based on the measured or apparent relative abundance of microlites and glass. We also define three classes based on dominant sizes of clinopyroxene (cpx) and oxide (ox) microlites (Table 3). Plagioclase is not used in the size classification because it can vary greatly in size and habit within a single clast.

A weak inverse correlation between vesicularity and microlite crystallinity is observed for both phases C and E. The high density clasts are mostly holocrystalline with euhedral tabular and prismatic microlites. The

lowest microlite number densities are associated with the coarsest microlites, which occur in the dense clasts from the close of Plinian phase C. Clusters and patches of extremely fine (<0.3 μm) clinopyroxene and oxide grains are irregularly distributed between the coarser microlites.

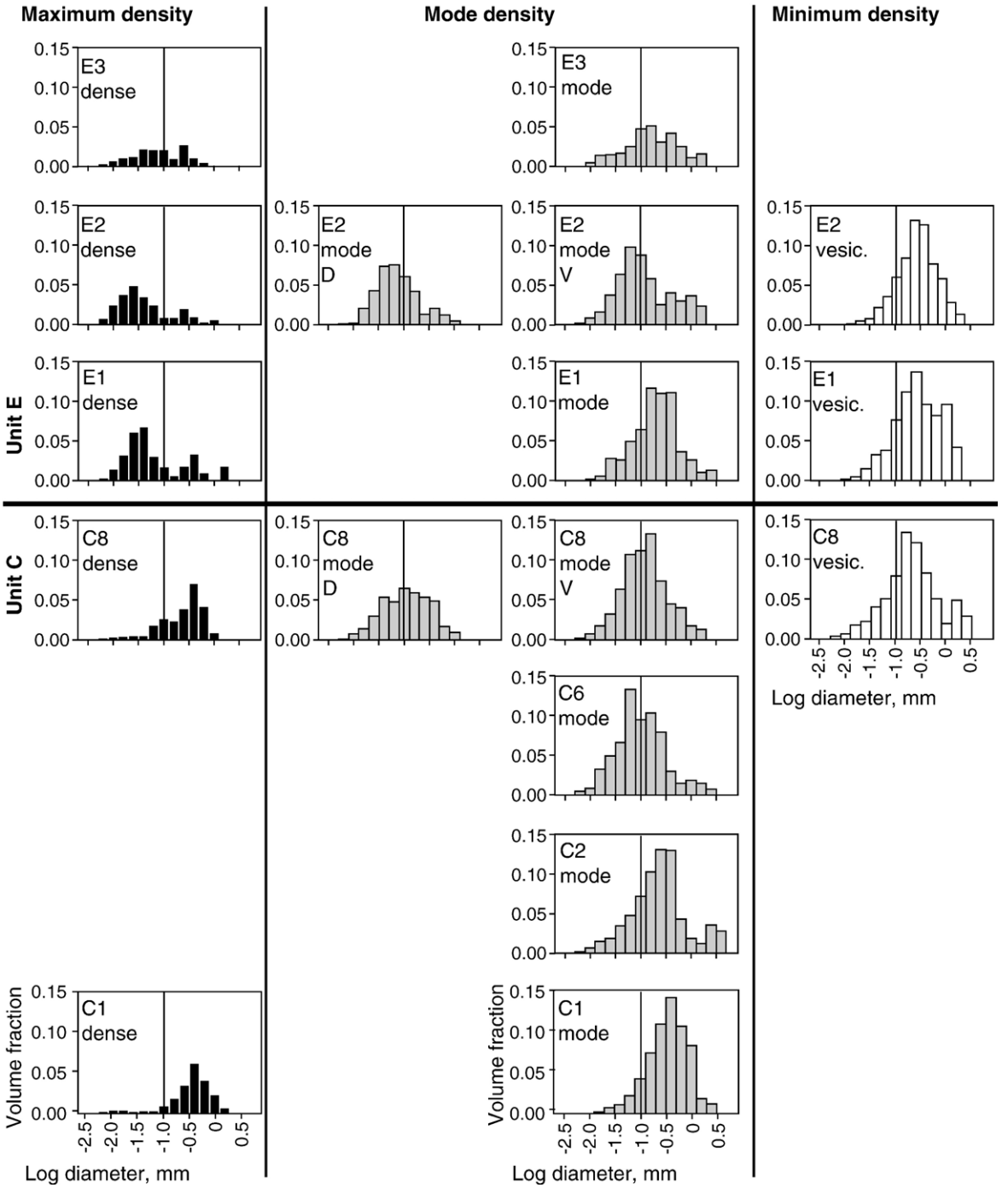

Fig. 6. Histograms of volume fraction vesicles with vesicle size arranged according to stratigraphic height. For samples with multiple modes, the more vesicular modes (mode V) are in right column, secondary denser modes (mode D) in left. Vertical lines are drawn at 0.1 mm equivalent diameter to assist comparison.

Most of the modal and minimum density clasts are hypocrystalline. Clasts from unit C typically contain fine-grained microlite populations, with thin needles of plagioclase and blades of clinopyroxene occurring alone or in radiating fans and bundles (Fig. 7a, b). Microlites in clasts from phase E have more euhedral habits (Fig. 7e, f). Fe–Ti oxide has an equant subhedral to euhedral habit in nearly all clasts, but size and number density vary slightly. Most of the modal clasts also contain pockets of very fine-grained crystals similar to those described for the high density clasts (Fig. 7e). At high magnification, the glassy matrix appears mottled and seems to be a collection of tiny crystallites with poorly resolved boundaries.

4. Interpretations

4.1. Interpretations of macroscopic data

Changes in median grain size with stratigraphic height are a useful proxy for changes in eruptive intensity with time (Fisher and Schmincke, 1984), assuming constant wind velocity and in the absence of significant shifts in clast density (Fig. 3). The grain size data suggest that during phase C, the eruption built rapidly to a relatively powerful intensity (represented by sample C2), then entered a period of fluctuating and somewhat weaker intensity depositing alternating beds of coarser and finer lapilli (samples C3, C4, C5). This was

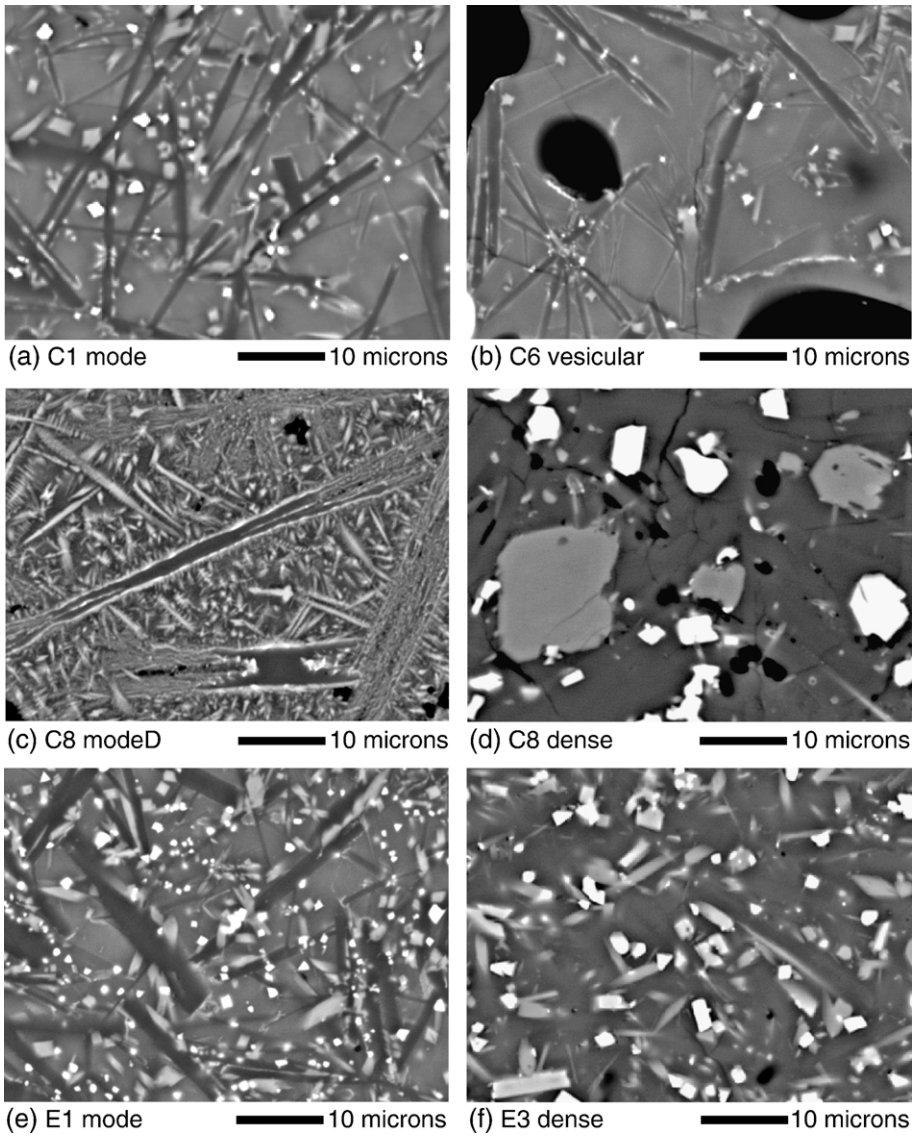

Fig. 7. Selected SEM images showing microlite textures. Mode D indicates the denser of two modes for sample C8.

Table 3
Summary of microlite textures observed in thin sections of representative 16–32 mm clasts

Sample	Clast	Density category	Vesicles (vol.%)	Apparent crystallinity	Apparent grain size	Microlites (# mm^{-2})	Groundmass (vol.%)				Typical size (μm)			Textural features present				
							Glass	Plag	Cpx	Ox	Plag	Cpx	Ox	Skeletal	Radiate	Dendrite	Needle	Incip
C1	20	Vesicular	70	Hypohyaline	Medium	1.8e+05	45	30	21	4	12	1.6	0.72		×		×	
C6	33	Vesicular	73	Hypohyaline	Medium	9.9e+04	57	23	20	1	14	3	1.2		×		×	
C8	72	Vesicular	71	Hypocrystalline	Medium	1.5e+05	28	36	35	0.2	12	0.8	0.6	×	×	×	×	
E1	14	Vesicular	74	Hypocrystalline	Fine	3.0e+05	22	47	28	3	10	1.8	0.6	×	×	×	×	
E2	68	Vesicular	65	Hypocrystalline	Fine–med						13	2.6	0.72	×	×	×	×	×
C1	18	Mode	63	Hypocrystalline	Medium	2.0e+05	33	35	28	3	9	2.2	0.8				×	
C2	35	Mode	70	Hypocrystalline	Fine	2.8e+05	11	48	39	2	8	1.4	0.6		×	×	×	×
C6	23	Mode	67	Hypocrystalline	Fine–med	2.8e+05	22	38	39	0.4	8	2.8	0.8			×		
C8	44	Mode V	67	Hypocrystalline	Fine	3.1e+05	14	54	31	1	12	2	0.6		×	×	×	×
C8	35	Mode D	41	Holocrystalline	Fine						20.8	8	0.24			×		×
E1	2	Mode	61	Hypocrystalline	Fine	3.1e+02	30	37	29	4	8	2.6	08				×	
E2	22	Mode V	53	Hypocrystalline	Fine	5.2e+05	10	54	34	2	3.6	2.2	0.72		×		×	×
E2	40	Mode D	37	Hypocrystalline	Fine–med						10	3	1		×		×	×
E3	21	Mode	30	Hypocrystalline	Medium	2.2e+05	17	49	31	3	12	2.2	1.2		×		×	
C1	29	Dense	22	Holocrystalline	Medium	4.8e+05	0	42	55	3	10	2.4	0.8		×	×		×
C2	59	Dense 1	47	Hypocrystalline	Fine						16	1.2	0.6		×		×	
C2	20	Dense 2	42	Hypocrystalline	Fine	2.9e+05	23	40	36	1	7.2	1.2	0.6		×	×	×	×
C6	4	Dense 1	48	Hypocrystalline	Fine	2.9e+05	12	45	43	0.2	8	2	0.6		×	×	×	
C6	31	Dense 2	48	Hypocrystalline	Medium						3	0.36	0.36				×	×
C8	81	Dense 1	26	Holocrystalline	Coarse	1.1e+02	0	69	22	8	>48	2	1.6					
C8	21	Dense 2	24	Hypocrystalline	Coarse	1.4e+02	31	41	23	5	>50	8	2.2	×				
E1	31	Dense	32	Holocrystalline	Fine	2.8e+05	0	67	29	4	10	3.2	0.6	×				×
E2	45	Dense	25	Holocrystalline	Fine						8	2	0.8	×				×
E3	11	Dense 1	16	Holocrystalline	Medium													
E3	27	Dense 2	3	Hypocrystalline	Fine	7.0e+05	9	51	38	2	4	2	0.4		×			×

Clasts are grouped by density: vesicular=lowest density clast of a sample; mode V=the more vesicular of two modes; mode D=the denser of two modes; dense 1=highest density clast of a sample; dense 2=second densest clast of a sample.
Apparent grain size categories: fine=cpx <2.5 μm (up to 11 μm), ox <0.7 μm (up to 3.0 μm); medium=cpx 2.0–3.0 μm (up to 12 μm), ox 0.8–1.4 μm (up to 4.0 μm); coarse=cpx 3.0–8.0 μm (up to 20 μm), ox 1.5–2.2 μm (up to 6.0 μm). Incip=incipient crystals, i.e. tiny poorly formed crystallites.
All clasts have some microlites outside these ranges, but classes are based on the most dominant sizes.

followed by a second period of more vigorous sustained eruption centered around sample C6, which represents the maximum eruptive intensity. Intensity decreased sharply at the close of phase C (sample C8). Phase E built quickly to its peak intensity, represented by the relatively coarse and well sorted samples E1 and E2. This intensity was maintained, apart from a minor waning interval, until nearly the end of the phase when it declined rapidly (sample E3).

Variations in lithic wall rock content of pyroclastic fall deposits suggest possible variations in the intensity of the eruption and/or the degree of involvement of external water (Fisher and Schmincke, 1984). For the 122 BC Plinian phases, increases in lithic content do not necessarily indicate increases in external water involvement, because they are not accompanied by decreases in median diameter or increases in fine ash content, which would be expected from onset of interaction with water. Instead, median grain size tends to increase with increasing lithic content (Fig. 3). We infer that the Plinian phases were essentially dry, and that more wall rock was incorporated during periods of higher eruption intensity due to enhanced scouring of the sides of the conduit. Similarly, the concurrent decreases in grain size and lithic content at the close of each Plinian phase indicate declining eruptive vigor and reduced capacity to incorporate and transport large clasts (e.g., samples C6 to C8 and E2 to E3).

The lack of quench textures and other features typical of phreatomagmatic clasts (Heiken and Wohletz, 1985) further supports the interpretation that the 122 BC Plinian phases were dry. The lack of highly fluidal clast morphologies suggests that at the time of fragmentation, the 122 BC magma was probably more viscous than magmas in typical low-intensity basaltic eruptions. The observed blocky to ragged clast morphologies are interpreted to result from tearing apart of viscous yet fluidal magma. The shift in dominant clast morphology from viscous/fluidal to brittle at the end of phase E is a vivid indication that significant changes in melt rheology accompanied the close of sustained explosive eruption.

Changes in clast density/vesicularity distributions are broad indicators of changes in the extent and style of

degassing in the conduit (e.g., Houghton et al., 2000; Gurioli et al., 2005; Adams et al., 2006). For example, the sharp high vesicularity peak of the density histogram for sample C6 (Fig. 3) suggests that, at the intensity maximum, the entire width of the conduit was occupied by relatively uniform, actively vesiculating magma. The shift toward high density in upper unit E indicates substantial gas loss from the erupting magma. Our results support Houghton et al.'s (2004a) inference that the tails or secondary modes of dense clasts on all the density histograms imply physical heterogeneity in the magma that approached the fragmentation surface at a given time. This heterogeneity was most pronounced at the ends of phases C and E, but was also significant at the start of C (Fig. 3). We caution that interpretations based on clast vesicularity alone are partly speculative. Detailed microtextural studies are used to evaluate and enhance these interpretations to provide a more complete picture of the vesiculation processes.

4.2. Interpretations of vesicle size and shape data

The modal and minimum density clasts of samples C1 through E2, as well as the maximum density clasts of samples C1 through C6, are dominated by convex and rounded polylobate bubble shapes (Fig. 4a, b). The complex shapes of bubbles in the 122 BC clasts are best explained by bubble coalescence (Gaonac'h et al., 1996a, 2005). The maximum density clasts of samples C8, E1, and E2, and both the modal and maximum density clasts of sample E3, are dominated by smaller bubbles with more angular and wrinkled contours (Fig. 4d, e, f). This suggests that, starting in late phase C, bubble coalescence was followed by some process of bubble collapse or shrinkage in parts of the magma.

Large and moderately sized bubbles have the most complex shapes in the 122 BC clasts, but even the smallest bubbles are not perfectly spherical, although they might be expected to have shorter and simpler growth histories and thus simpler shapes. This pattern appears in clasts from every stratigraphic level and suggests that coalescence became important very early in the magma's ascent. Coalescence may occur more easily and reach a more advanced stage in basaltic magmas than in more silicic magmas due to the lower viscosity of basaltic melt (Herd and Pinkerton, 1997). The evidence for extensive coalescence implies that the maximum bubble number densities were even higher than the already high values indicated by our measurements. Possible reasons that the coalesced bubbles failed to relax to spherical shapes include a short time scale due to rapid ascent of the 122 BC magma, and relatively high effective viscosity of the magma (Herd and Pinkerton, 1997). In contrast to the patterns in the Etna 122 BC clasts, the larger (cm-sized) bubbles in Strombolian scoria have complex shapes and are commonly connected in chains indicating substantial coalescence, but the smaller (mm-sized) bubbles are spherical (Lautze and Houghton, 2005; B.F. Houghton, unpublished data).

Bubble number densities in the modal density clasts vary by less than an order of magnitude (Table 2), suggesting that most of the melt experienced similar nucleation conditions. Differences in bubble size, shape, and spacing become more pronounced in samples from higher stratigraphic levels, especially in the densest clasts. We suggest below that these variations were produced by late stage processes in the upper conduit after a common early ascent history.

The bubbles in the Etna 122 BC clasts range down to much smaller sizes than in other basaltic ejecta (e.g., Mangan and Cashman, 1996; Simakin et al., 1999; Lautze and Houghton, 2005), suggesting that the interval of bubble nucleation may have extended until close to fragmentation (Blower et al., 2002). Alternatively, the influences of growth and coalescence of bubbles may have been increasingly restricted due to increasing viscosity and crystallinity of the ascending magma. Careful observations of clasts in thin section show that the largest bubbles are not concentrated at the centers of clasts, but are distributed uniformly throughout the clasts. We infer that post-fragmentation expansion was not an important factor in the development of the largest bubbles in the 16–32 mm diameter clasts that make up our density samples.

The unusually high bubble number densities and small bubble sizes in the Etna 122 BC clasts suggest that the bubble nucleation rate was probably much faster than the rates in Hawaiian or Strombolian eruptions. Such rapid bubble nucleation occurs at high supersaturation pressures, which equate to high rates of decompression (Sparks, 1978; Navon and Lyakhovsky, 1998; Mangan and Sisson, 2000; Mangan et al., 2004). Rapid decompression and ascent have been proposed for the 122 BC magma by Coltelli et al. (1998) and Del Carlo and Pompilio (2004). Our microtextural data confirm that a high ascent rate was an important factor in causing the 122 BC eruption to reach Plinian intensity.

Vesicle or bubble size distributions (VSDs or BSDs) may be plotted and analyzed in several ways to show the mathematical relationship between bubble number density and size, and the best-fit trends give information about conduit processes (Toramaru, 1989; Toramaru, 1990; Mangan et al., 1993; Cashman and Mangan, 1994;

Klug and Cashman, 1994; Gaonac'h et al., 1996a,b; Mangan and Cashman, 1996; Simakin et al., 1999; Blower et al., 2001, 2002; Klug et al., 2002; Polacci et al., 2003; Gaonac'h et al., 2005; Gurioli et al., 2005; Toramaru, 2006). Some researchers interpret exponential trends in VSDs based on a steady-state population density function (e.g., Mangan et al., 1993; Cashman and Mangan, 1994; Klug and Cashman, 1994; Mangan and Cashman, 1996). Other workers report power law VSDs, but there is no consensus on the best formulation of the power law (e.g., Gaonac'h et al., 1996a,b; Simakin et al., 1999; Blower et al., 2001; Blower et al., 2002; Klug et al., 2002). We follow Blower et al. (2001, 2002) in using the form $N_V{>}R{=}AR^{-d}$, where R is bubble radius (in mm), $N_V{>}R$ is the cumulative number density of bubbles (in mm^{-3}) with radii larger than R, A is a constant of proportionality, and d is the power law exponent.

For the 122 BC vesicle data, power laws with exponents ranging from d=2.7 to 2.9 give better fits than exponential trends (Fig. 8). Two contrasting models have been proposed to explain power law VSDs (Gaonac'h et al., 1996a,b; Blower et al., 2001, 2002), but they cannot be distinguished based on d alone. Both models are probably simplified, and the physical meaning of power law exponents for natural bubble populations is still not clear. In light of these ambiguities, we report our power law fits for the purpose of comparison with data from other eruptions, but we do not emphasize the significance of the VSDs in our subsequent interpretations.

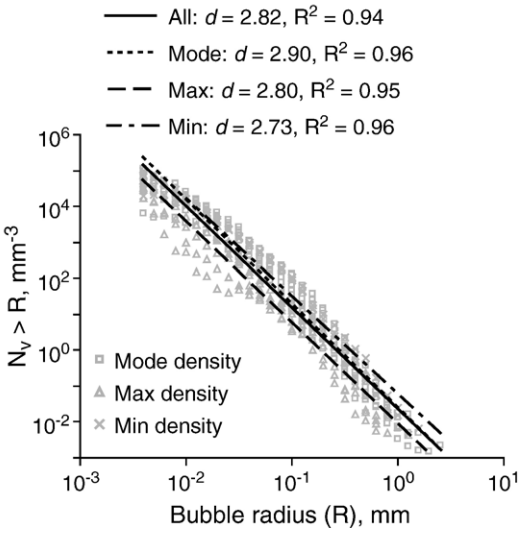

Fig. 8. Plot of cumulative volumetric bubble number density ($N_V{>}R$) against equivalent bubble radius (R) in bilogarithmic coordinates. Power law trends fit the data better than exponential or other trends. Values of exponents (d) are indicated.

The drastic (30–50%) drop in vesicularity and the decrease in modal bubble size through phase E indicate a significant role for outgassing, i.e., loss of the gas phase. In Strombolian eruptions, outgassing is accomplished when large coalesced bubbles rise through relatively stationary melt, intersect the free surface, and burst to release their gas (Vergniolle and Mangan, 2000). However, the high microcrystallinities observed in the Etna 122 BC clasts suggests that this magma was too viscous for gas bubbles to move easily relative to the melt in the shallow conduit.

We suggest instead that the angular, pinched shapes of the bubbles in the high density samples of phases C and E are consistent with processes of permeability development followed by bubble collapse. Experiments on vesicular basalt and hydrated rhyolite show that bubble coalescence creates interconnected pathways through which gas can escape, causing shrinkage and distortion of bubbles (Saar and Manga, 1999; Burgisser and Gardner, 2005). Microfractures and tiny void spaces between microlites may also bridge areas between bubbles to promote permeability (Walker, 1989; Saar, 1998). Such connections among bubbles may be obscured after gas loss as bridging pore spaces can collapse (Saar, 1998). Permeability can affect some parts of the magma while adjacent parts remain impermeable (Klug and Cashman, 1996). We do not attribute the bubble collapse to gravity or shearing because the collapsed bubbles do not align in any preferred orientation.

4.3. Interpretations of microlite textures

Vesicle and microlite data are summarized and matched with stratigraphic height in Fig. 9. For our interpretations of the 122 BC microlite textures, we follow current models for Plinian eruptions in assuming that rapid ascent precludes significant undercooling through heat loss in the conduit (e.g., Jaupart, 1996; Papale, 1998). The effective undercooling that triggers microlite formation arises instead from an increase in the thermodynamic stabilities of anhydrous mineral phases in response to decompression and dehydration (Lipman and Banks, 1987; Geschwind and Rutherford, 1995).

We also assume that the sampled lapilli were quenched in the plume and no further crystallization occurred after clasts left the vent. Experiments and models relating to the cooling of pyroclasts in plumes (Tait et al., 1998; Hort and Gardner, 2000) show that the time scale of quenching depends on the size of the clast. The glass transition temperature for Etna basalt, calculated as the temperature at which the melt's viscosity reaches 10^{11} Pa s, is 982 K (Giordano and Dingwell, 2003). In 2–3 cm lapilli, the

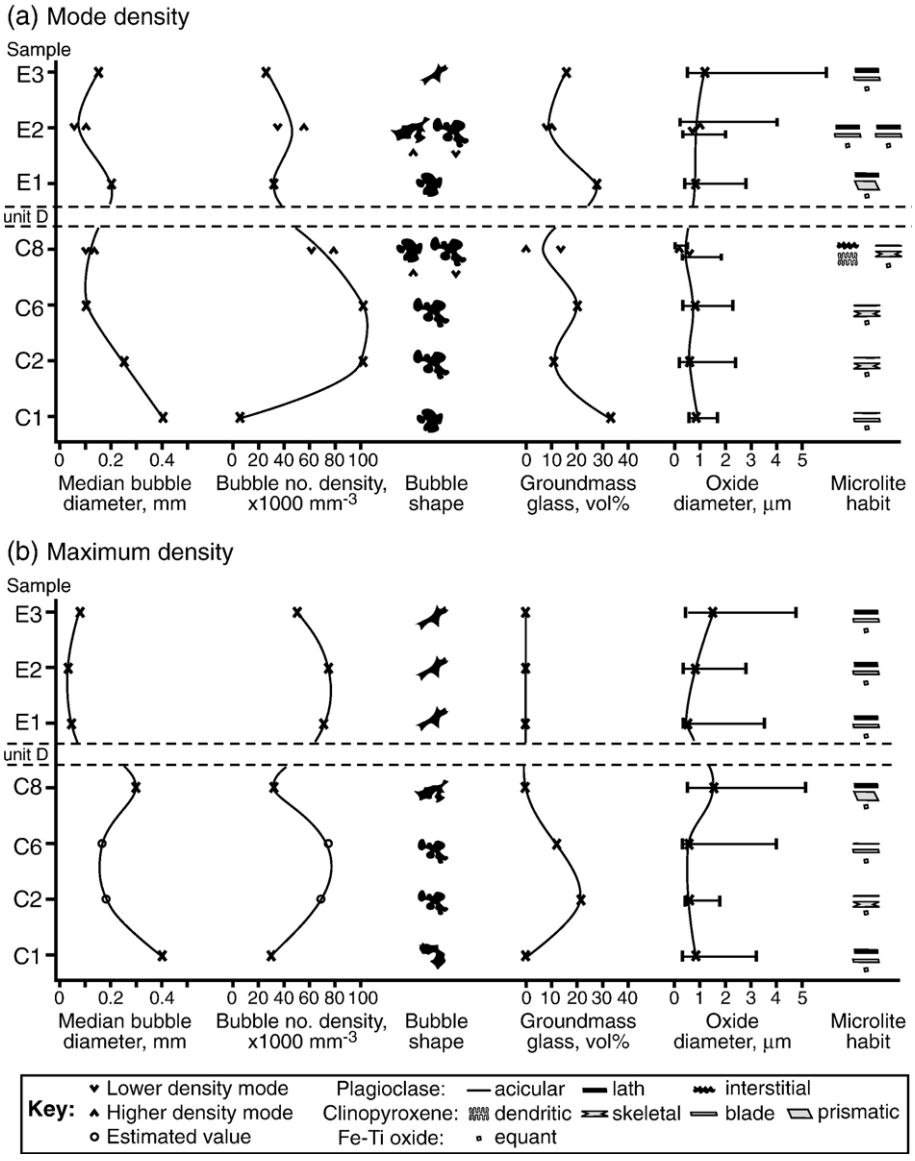

Fig. 9. Summary diagram of bubble and crystal data for (a) modal and (b) maximum density clasts of units C and E. Only the most dominant bubble shapes and crystal habits are indicated; every clast has a range. For size of Fe–Ti oxide microlites, X marks typical size and bars indicate range. Open circles indicate estimated values that were not quantified as rigorously as the rest.

clast diameter that we used for microtextural studies, the rims take 10 s to cool from an eruption temperature of 1100 K to the glass transition temperature, and the centers reach this temperature within 150 s (Hort and Gardner, 2000). This time interval is too brief for significant post-fragmentation crystallization to occur in clasts of this size.

Microlite nucleation rates cannot be estimated quantitatively with the available data. Crystal number density is not a foolproof indicator of nucleation rate for two reasons. Firstly, estimation of a rate requires a constraint on the time interval. The great textural heterogeneity in the Etna 122 BC magma near the point of fragmentation suggests different ascent histories for different parts of the magma. We cannot assume that the time available for crystallization was the same for all the magma, and thus we cannot assume that differences in crystal number density directly reflect differences in nucleation rate. For example, the relatively low number density of microlites in the mode and minimum density clasts of most of phase C (Table 3; Fig. 7a, b) could suggest a low nucleation rate, but they more likely reflect short residence time in the conduit. Secondly, the

observed groundmass textures reflect the conditions for only the final stage of ascent before fragmentation. Other conditions may have prevailed earlier in the magma's history, but evidence of those earlier conditions may become obscured or overprinted by changes in the upper conduit. Experiments on analog materials show that the crystal texture of a rock can transform dramatically if the magma is held at a temperature near the solidus for some time (Means and Park, 1994). The time scale for such crystal ripening is days for a high-silica melt (Hammer and Rutherford, 2002) and probably much shorter for basaltic melts with lower viscosity and higher component diffusivity (Zhang and Stolper, 1991; Zhang and Behrens, 2000).

The patches of very small microlites common in the highly crystalline clasts probably represent a second stage of crystal nucleation at a high level in the conduit. The crystallites that impart a mottled look to the glassy matrix of more crystalline clasts are also interpreted as late-nucleating crystals that had a limited growth time. Taddeucci et al. (2005) observe evidence for a second microlite nucleation in clasts from Strombolian-style eruptions of Etna, and suggest that it was triggered by cooling during a long (hours to days) residence time in the conduit. The time scale for the 122 BC Plinian eruption was much shorter, so we suggest that if a second microlite nucleation did occur, it was triggered instead by exsolution of the last H_2O from the melt, possibly accompanying pressure drop due to the downward propagation of the fragmentation wave (Cashman et al., 2000).

If interpreted cautiously, crystal size may give some information about rates and time scales of crystal growth. Fe–Ti oxide microlites are likely to give the most reliable constraints because their growth rate is relatively insensitive to H_2O content. Assuming constant temperature throughout most of the magma's ascent, the main factor governing size of Fe–Ti oxide crystals is the time interval available for growth. The modal clasts from unit C share a relatively consistent range of crystal size (Fig. 9a). The size range is wider in the maximum-density clasts of phase C (Fig. 9b). In phase E, all clasts are dominated by relatively coarse (e.g. cpx up to 20 μm) microlites, and the textural contrast between modal and maximum density clasts is diminished. We infer that by the end of the second Plinian phase, all the remaining melt had resided in the conduit for a considerable time. A weakness of these interpretations is that they assume constant crystal growth rate, which is unlikely to apply to all the magma.

Crystal habit depends on the relative rates of processes such as diffusion of chemical components, diffusion of heat, and attachment of atoms to crystal surfaces (Kirkpatrick, 1981). Diffusion-controlled growth, associated with large degrees of undercooling and strong disequilibrium, produces spherulitic and dendritic crystal habits (Lofgren, 1974). Microlite habits characteristic of disequilibrium occur in the minimum and modal density clasts of all samples of Plinian phase C (Fig. 7a, b, c; Fig. 9a). Similar textures to these were observed in basalt crystallization experiments at undercoolings of 30–70 °C (Lofgren, 1974). Modal clasts with high number densities of small crystals (Fig. 7e) are inferred to have experienced high nucleation rates and low to moderate growth rates, indicating high undercooling. The clast from the secondary density mode of sample C8 (Fig. 7c) has microlites with textures suggesting very fast growth, but nucleation rate is poorly constrained because the number density of the complex dendritic crystals cannot be determined reliably. Minimum density clasts with low number densities of acicular and skeletal crystals (Fig. 7b) are interpreted to have had high growth rates and either low nucleation rates (in which case the undercooling was moderately low) or very short residence times (associated with fast ascent and high undercooling).

Of the maximum density clasts, only samples C2 and C6 have microlites with disequilibrium habits, including acicular plagioclase and skeletal and elongate clinopyroxene (Fig. 9b). The rest of the maximum density clasts are dominated by more prismatic or tabular microlites that do not indicate such rapid diffusion-controlled growth. We infer that dense clasts with lower numbers of coarse subhedral crystals (Fig. 7d) experienced fairly high growth rates but low nucleation rates, indicating the lowest degrees of undercooling over a prolonged interval. The maximum density clast of sample C8 has exceptionally large microlites with equant and euhedral habits, indicating slow growth in relatively steady conditions for at least the last portion of that magma parcel's history (Kirkpatrick, 1981).

4.4. Combined interpretations

4.4.1. Rapid ascent

The high bubble number densities indicate rapid bubble nucleation at high H_2O supersaturation. The small bubble sizes suggest that bubbles had limited opportunity to grow. The high number densities of microlites in most clasts of unit C suggest a dominance of crystal nucleation over growth, consistent with large degrees of undercooling. Disequilibrium microlite habits in many samples also suggest large undercooling. Due to the short time scale of ascent in the Plinian eruption, this

undercooling is most likely induced by rapid devolatilization, rather than by conductive heat loss.

All of these interpretations indicate that the 122 BC magma was subjected to rapid decompression associated with rapid ascent. Coltelli et al. (1998) suggest that flank deformation induced sudden decompression, leading to a surge of bubble nucleation that propelled rapid ascent. Our microtextural data do not specifically support or disprove this hypothesis, and it is one viable cause of the high rate of bubble nucleation. Another possible cause arises from recent work on the primitive magmas of Etna's 2001 and 2002–03 flank eruptions, which are chemically similar to the 122 BC magma (Métrich et al., 2004). When melt inclusion analyses for several elements are combined and compared with models, the results suggest that the initial dissolved CO_2 in the 2002 and 2002–03 magmas is at least 1.5 wt.%, much higher than previously thought (Papale et al., 2006; Spilliaert et al., 2006). Much of this CO_2 is lost through early open system degassing at depths of >9 km (Spilliaert et al., 2006). By analogy, we suggest that early formation of CO_2 bubbles could have accelerated the 122 BC magma upward by increasing the magma's volume and buoyancy. Sufficiently fast ascent could have led to supersaturation in H_2O. In this model, dehydration accompanying the CO_2 loss could have induced early microlite crystallization, increasing the H_2O concentration in the melt and further encouraging H_2O supersaturation. The early presence of microlites also would have increased the magma's effective viscosity, so that when rapid H_2O exsolution occurred, the gas and melt would remain coupled.

4.4.2. Conduit residence time

Our microtextural results are consistent with Houghton et al.'s (2004a) preliminary interpretation, based on clast density distributions, that conduit residence time was a critical factor in creating a wide range of bubble and microlite textures in the 122 BC magma. Our detailed vesicle and microlite characterizations allow us to describe the effects of contrasting residence times throughout the eruption.

The modal density clast from sample C1 has an atypically low vesicularity for unit C and a low number density of coarse, widely spaced bubbles (Figs. 4a; 9a) that resemble textures in typical Strombolian scoria (e.g., Lautze and Houghton, 2005). We suggest that the melt ejected in the earliest stage of phase C had been in the conduit since the end of Strombolian phase A, and thus had time to develop relatively mature vesicle textures.

The high bubble number densities, small bubble sizes, and skeletal microlite habits that dominate samples C2 and C6 (Fig. 4b) support an interpretation of shorter conduit residence time and rapid bubble nucleation due to high rates of ascent and decompression. Microlite crystallinity generally increases through unit C, and the microlites in the modal clasts maintain a relatively constant average size with acicular and skeletal habits indicating rapid growth. Dense clasts from samples in the middle of unit C have relatively small, widely spaced bubbles with complex polylobate shapes. These characteristics could develop through an extended period of coalescence and gas loss. Sample C8, from the closing stage of phase C, features a sharp reduction in bubble number density and very complex bubble shapes in both of its modal density clasts and its high density clast, indicating advanced coalescence and outgassing (Figs. 4d; 9a,b). The groundmass textures of the dense clasts progressively diverge from those of the equivalent modal clasts through the sequence of samples C2–C8, suggesting an increasing contrast in residence time between the portions of melt represented by the two subsets of clasts.

Between samples C8 (end of phase C) and E1 (start of phase E), bubble size and spacing increase while number density and complexity of shape decrease (Fig. 4c versus Fig. 4e). This combination of changes is consistent with an interval of stable near-equilibrium conditions in the magma that allowed some bubble growth, substantial coalescence, and possibly some relaxation of shape. Also, microlites become larger and less skeletal between samples C8 and E1 (Fig. 7c vs. Fig. 7e), suggesting a trend toward equilibrium crystal growth. We infer that at the end of the first Plinian phase, the magma slowed until it was effectively stationary in the shallow conduit for minutes to hours during the weak phreatomagmatic phase D.

Groundmass textures appear generally similar throughout unit E, in contrast with the wide range of textures in unit C. We attribute this to the stagnation that affected all the magma in the conduit during phase D. The contrasts in groundmass texture that had developed during mid to late phase C became subdued as the phase E magma was homogenized during a period of near-equilibrium crystallization under uniform conditions. Bubbles appear more shrunken and pinched in later samples (Fig. 4f), suggesting increasing importance of bubble collapse with longer residence time.

Houghton et al. (2004a) suggest that the highest degrees of outgassing and crystallization occurred in an annulus of slow-moving magma along the margins of the conduit. This idea is compatible with well-known models of pipe flow. The nature of pipe flow depends on the Reynolds number, defined as $Re=\rho VD/\mu$, where ρ is density of the fluid, V is mean velocity, D is pipe

Table 4
Parameters relevant to the Etna 122 BC magma used in estimation of the maximum Reynolds number ($Re_{max}=\rho_{max}V_{max}D_{max}/\mu_{min}$) at two points in conduit ascent

Variable	Estimate	Justification
Early in ascent (just after bubble nucleation): $Re_{max}=4860$		
Density (ρ_{max})	2430 kg m^{-3}	Calculated for melt density of 2700 kg m^{-3} and 10% vesicularity
Velocity (V_{max})	1 m s^{-1}	Typical ascent rate (Rutherford and Gardner, 2000)
Conduit diameter (D_{max})	20 m	Common width of basaltic dikes
Viscosity (μ_{min})	10 Pa s	Hot crystal-free basaltic melt (Giordano and Dingwell, 2003)
Late in ascent (just before fragmentation): $Re_{max}=170$		
Density (ρ_{max})	850 kg m^{-3}	Modal clast density at intensity maximum (sample C6)
Velocity (V_{max})	100 m s^{-1}	Maximum estimate (Papale et al., 1998)
Conduit diameter (D_{max})	20 m	Common width of basaltic dikes
Viscosity (μ_{min})	10^4 Pa s	Minimum viscosity of basaltic melt with 60% microlites (Pinkerton and Stevenson, 1992)

diameter, and μ is viscosity (Munson et al., 1990). For $Re<2100$, pipe flow is typically laminar and Poiseuille flow theory predicts a parabolic velocity profile with the maximum speed along the pipe's central axis. For $Re>4000$, pipe flow is turbulent, and the velocity profile is described by an empirical power-law relationship within certain limits (Munson et al., 1990). Intermediate *Re* numbers are associated with a transition between laminar and turbulent flow.

Assuming steady flow of a fluid with Newtonian rheology through a smooth cylindrical conduit, we estimate the maximum *Re* for the Etna 122 BC magma at two points: just after bubble nucleation but before significant bubble growth, and just before fragmentation (Table 4). Our maximum *Re* at depth exceeds 4000, indicating turbulent flow. Higher in the conduit, the magma's effective viscosity increases with increasing microlite content (Pinkerton and Stevenson, 1992; Lejeune and Richet, 1995), and the Reynolds number drops below 200. In addition to the effect of microlites, the bubbles probably also increase the effective viscosity because they show no evidence of strain (Llewellin et al., 2002). Therefore the viscosities in Table 4 are minimum estimates, and we suggest that laminar flow is likely for most of conduit ascent. However, we recognize that we use simplifying assumptions and uncertain parameters, and that pipe flow commonly departs from ideal conditions (Kerswell, 2005), so the flow may approach the turbulent transition. Turbulent flow adds complications including a radial component to velocity that may lead to mixing and enhanced bubble interactions (H. Gonnermann, personal communication, 2006).

Laminar and turbulent time-averaged velocity profiles are shown in Fig. 10a. Both types of flow have slower-moving zones along the margins, with the important consequence that melt near the margins would have an extended conduit residence time, with the potential to develop more mature vesicle and microlite textures. Parcels of magma that travel through conduits with such velocity profiles yet fragment at the same moment must have traveled along different flow lines with different ascent rates, and experienced different degassing and crystallization histories (Fig. 10b, c). For example, melt that follows path 1 in Fig. 10 would be subjected to a shorter rise time and higher

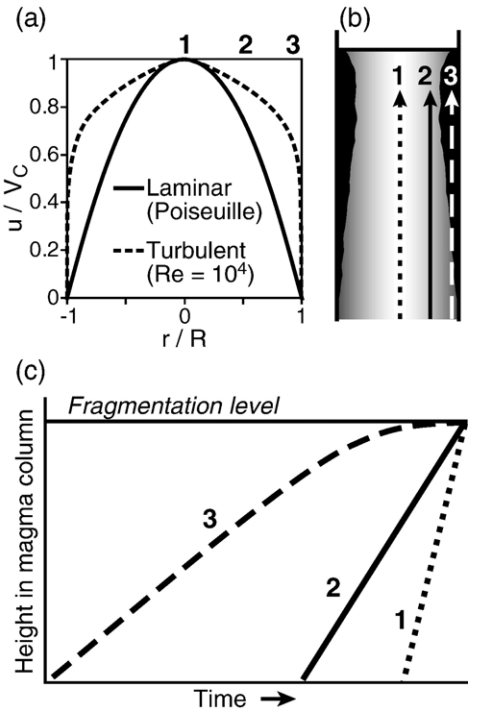

Fig. 10. (a) Calculated and empirical velocity profiles for laminar and turbulent flow of a steadily flowing Newtonian fluid in a pipe, after Munson et al. (1990). Normalized velocity and normalized conduit radius are indicated by u/Vc and r/R, respectively. (b) Cartoon of the upper conduit with faster moving magma in lighter gray and stagnant magma in black. (c) Schematic plot of height with time. Bold numbers **1**, **2**, **3** in each part of the figure indicate magma parcels following three idealized paths assuming laminar flow. Parcel 1 rises rapidly along the center and experiences the highest decompression rate. Parcel 2 rises more slowly and thus must have entered the conduit at an earlier time in order to be erupted simultaneously with 1. Parcel 3, having entered the conduit much earlier, rises relatively slowly and stagnates in the upper conduit, where it undergoes near-equilibrium degassing and crystallization before being ejected along with 1 and 2.

decompression rate and would produce more vesicular clasts, while melt that travels along the slower path 3 would experience a closer approximation to equilibrium degassing and crystallization and would produce clasts with more mature populations of crystals and bubbles. As the magma parcels rise to shallower depths, the differences in velocity and residence time between the axial (path 1) and marginal (path 3) zones increase, and textural contrasts also become more acute with time.

4.4.3. Narrative model for the Etna 122 BC eruption

The first activity in the 122 BC eruption (phase A) was Strombolian, not Plinian (Coltelli et al., 1998). Some of the magma involved in the Strombolian explosions remained in the conduit when the activity switched to weak phreatomagmatic explosions (phase B). The residual slow-rising magma was the first material to be ejected in Plinian phase C. The evidence for intensity fluctuations during early phase C suggests that coupling between the gas and melt phases may have been difficult to maintain (Fig. 11a). Eruption intensity stabilized at a maximum in the middle of phase C (Fig. 11b).

Assuming laminar flow, a parabolic velocity profile across the conduit caused a divergence in behavior between axial and marginal melt. Magma along the central axis maintained at least partially coupled degassing behavior and ascended too rapidly for much crystallization to occur, while material along the conduit walls moved slowly enough to permit significant crystallization, permeability development, and outgassing. As phase C continued, the contrasts between marginal and axial zones of the conduit became more pronounced, and the proportion of highly outgassed magma increased (Fig. 11c). The fragmentation surface was still dominated by the more gas-rich, less crystalline magma near the conduit axis, but a lesser and variable proportion of the fragmentation surface also intersected the more outgassed, crystalline melt along the margins.

As proposed by Houghton et al. (2004a,b), stagnation and accumulation of magma along the conduit margins led to a reduction in the effective radius of the conduit in an extension of the model proposed by Wilson et al. (1995) for Hawaiian explosions. The eruption intensity waned as the ongoing explosion was forced to remove increasingly large quantities of this obstructing material. Plinian phase C ended when the buildup of dense crystalline material reduced the conduit radius to the point that rapid ascent could not be sustained (Fig. 11d).

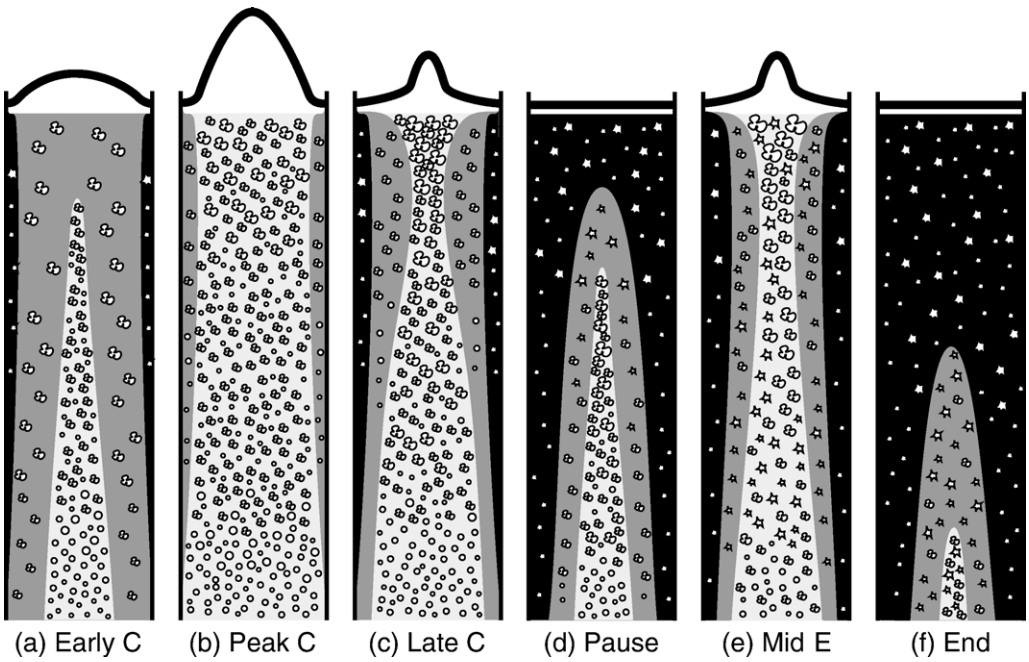

Fig. 11. Cartoons depicting the conduit at different stages of the 122 BC eruption. Curved lines along top schematically represent laminar velocity profiles near the fragmentation surface. Lighter gray is less dense, more gas-rich magma; black is stagnant, degassed magma. Bubble shapes are drawn to represent extent of coalescence and collapse. (a) Early in phase C, slow-moving magma from the previous Strombolian phase was cleared out. (b) At the peak of C, almost the full width of the conduit was occupied by fast-moving, rapidly vesiculating magma. (c) Accumulation of stagnant material late in phase C led to (d) a pause in Plinian eruption (phase D). (e) Fast-moving magma reached the fragmentation surface again in phase E, but (f) the conduit quickly became blocked again, leading to the termination of the eruption.

During the pause and the shallow phreatomagmatic explosions of phase D, the melt left in the conduit underwent additional bubble coalescence and collapse and microlite crystallization. This holding period reduced some of the textural differences that had developed across the conduit during phase C. Removal of the blockage was achieved by passive fragmentation with the aid of external water and/or by mingling with adjacent faster-moving material.

Plinian eruption resumed with the start of phase E, but because melt and gas were already decoupled to some extent in most of the magma, the processes of crystallization, outgassing, and stagnation took effect more rapidly and became more fully developed than in phase C (Fig. 11e). Finally, nearly all the magma was extensively outgassed, and the full width of the shallow conduit became blocked (Fig. 11f). This prompted a second switch to wet explosions (phases F and G), which were not followed by renewed Plinian eruption.

5. Conclusions

Data on pre-eruptive volatile content (Del Carlo and Pompilio, 2004) along with our microtextural evidence show that basaltic Plinian volcanism at Mt Etna in 122 BC was enabled by coupled degassing associated with high contents of CO_2 and H_2O and high rates of magma ascent, decompression, and bubble nucleation. Two possible causes for the rapid decompression that triggered Plinian activity are (1) a large and abrupt flank deformation causing unloading and an instantaneous conduit-wide decompression, or (2) an early nucleation of CO_2-dominated bubbles causing rapid ascent. In either case, the early fast decompression caused a high H_2O supersaturation in the melt and triggered very rapid nucleation of H_2O-dominated bubbles, leading to further acceleration of the magma. Early microlite crystallization probably increased the magma's effective viscosity and allowed coupled degassing to dominate in the most intense stages of the eruption. The next stage of this study will quantify ascent conditions through experiments in which samples of 122 BC melt are subjected to near-instantaneous, steady, and multi-stage decompressions.

The remarkable heterogeneity in bubble and groundmass textures found in a given stratigraphic interval shows that different processes became dominant in different portions of the magma following a shared initial history. We link this to a parabolic velocity profile across the conduit associated with approximately laminar flow. While bubbles continued to nucleate and grow in the rapidly ascending melt along the conduit axis, the slower melt along the conduit margins began to shift toward decoupled behavior, in which gas escaped upward and toward conduit walls through permeable networks of interconnected pore spaces. The marginal magma became increasingly outgassed and crystalline until it stagnated along the walls of the upper conduit. Accumulation of this sluggish magma reduced the conduit diameter and caused the decline of each Plinian phase.

Acknowledgements

This research was supported by NSF grants EAR01-25719 and EAR-5-37459. The draft manuscript was improved greatly with the help of constructive reviews by Gary Barnes, Helge Gonnermann, Julia Hammer, Andy Harris, Don Swanson, and Jacopo Taddeucci. The field program was generously funded by the Istituto Nazionale di Geofisica e Vulcanologia.

References

Adams, N.A., Houghton, B.F., Fagents, S.A., Hildreth, W., 2006. The transition from explosive to effusive eruptive regime: the example of the 1912 Novarupta eruption, Alaska. Geological Society of America Bulletin 118, 620–634.

Blackburn, E.A., Wilson, L., Sparks, R.S.J., 1976. Mechanisms and dynamics of strombolian activity. Journal of the Geological Society (London) 132, 429–440.

Blower, J.D., Keating, J.P., Mader, H.M., Phillips, J.C., 2001. Inferring volcanic degassing processes from vesicle size distributions. Geophysical Research Letters 28, 347–350.

Blower, J.D., Keating, J.P., Mader, H.M., Phillips, J.C., 2002. The evolution of bubble size distributions in volcanic eruptions. Journal of Volcanology and Geothermal Research 120, 1–23.

Branca, S., Del Carlo, P., 2004. Eruptions of Mt Etna during the past 3200 years: a revised compilation integrating the Historical and stratigraphic records. In: Bonaccorso, A., Calvari, S., Coltelli, M., Del Negro, C., Falsaperla, S. (Eds.), Mt. Etna: Volcano Laboratory. AGU Geophysical Monograph Series, vol. 143, pp. 1–27.

Burgisser, A., Gardner, J.E., 2005. Experimental constraints on degassing and permeability in volcanic conduit flow. Bulletin of Volcanology 67, 42–56.

Carey, S., Sparks, R.S.J., 1986. Quantitative models of fallout and dispersal of tephra from volcanic eruption columns. Bulletin of Volcanology 48, 109–125.

Cashman, K.V., Mangan, M.T., 1994. Physical aspects of magmatic degassing: II. Constraints on vesiculation processes from textural studies of eruption products. In: Carroll, M.R., Holloway, J.R. (Eds.), Volatiles in Magmas. Reviews in Mineralogy. Mineralogical Society of America, pp. 447–478.

Cashman, K.V., Sturtevant, B., Papale, P., Navon, O., 2000. Magmatic fragmentation. In: Houghton, B.F., McNutt, S.R., Rymer, H., Stix, J. (Eds.), Encyclopedia of Volcanoes. Academic Press, San Diego, pp. 421–430.

Chester, D.K., Duncan, A., Guest, J., Kilburn, C., 1985. Mount Etna, The Anatomy of a Volcano. Chapman and Hall, London. 406 pp.

Civetta, L., Galati, R., Santacroce, R., 1991. Magma mixing and convective compositional layering within the Vesuvius magma chamber. Bulletin of Volcanology 53, 287–300.

Coltelli, M., Del Carlo, P., Vezzoli, L., 1998. Discovery of a Plinian basaltic eruption of Roman age at Etna volcano, Italy. Geology 26, 1095–1098.

Coltelli, M., Del Carlo, P., Vezzoli, L., 2000. Stratigraphic constrains for explosive activity in the past 100 ka at Etna volcano, Italy. International Journal of Earth Sciences 89, 665–677.

Criswell, C.W., 1987. Chronology and pyroclastic stratigraphy of the May 18, 1980, eruption of Mount St. Helens, Washington. Journal of Geophysical Research 92, 10237–10266.

Del Carlo, P., Pompilio, M., 2004. The relationship between volatile content and the eruptive style of basaltic magma: the Etna case. Annals of Geophysics 47, 1423–1432.

Denlinger, R.P., Hoblitt, R.P., 1999. Cyclic eruptive behavior of silicic volcanoes. Geology 27, 459–462.

Dixon, J.E., Stolper, E.M., 1995. An experimental study of water and carbon dioxide solubilities in mid-ocean ridge basaltic liquids: 2. Applications to degassing. Journal of Petrology 36, 1633–1646.

Fierstein, J., Hildreth, W., 1992. The Plinian eruptions of 1912 at Novarupta, Katmai National Park, Alaska. Bulletin of Volcanology 54, 646–684.

Fisher, R.V., Schmincke, H.-U., 1984. Pyroclastic Rocks. Springer-Verlag, Heidelberg, Germany. 472 pp.

Froggatt, P.C., 1981. Stratigraphy and nature of Taupo Pumice Formation. New Zealand Journal of Geology and Geophysics 24, 231–248.

Gaonac'h, H., Lovejoy, S., Stix, J., Scherzter, D., 1996a. A scaling growth model for bubbles in basaltic lava flows. Earth and Planetary Science Letters 139, 395–409.

Gaonac'h, H., Stix, J., Lovejoy, S., 1996b. Scaling effects on vesicle shape, size and heterogeneity of lavas from Mount Etna. Journal of Volcanology and Geothermal Research 74, 131–153.

Gaonac'h, H., Lovejoy, S., Schertzer, D., 2005. Scaling vesicle distributions and volcanic eruptions. Bulletin of Volcanology 67, 350–357.

Garcia, M.O., Rhodes, J.M., Wolfe, E.W., Ulrich, G.E., Ho, R.A., 1992. Petrology of lavas from episodes 2–47 of the Puu Oo eruption of Kilauea Volcano, Hawaii: evaluation of magmatic processes. Bulletin of Volcanology 55, 1–16.

Garcia, M.O., Pietruszka, A.J., Rhodes, J.M., 2003. A petrologic perspective of Kilauea Volcano's summit magma reservoir. Journal of Petrology 44, 2313–2339.

Geschwind, C.-H., Rutherford, M.J., 1995. Crystallization of microlites during magma ascent: the fluid mechanics of 1980–86 eruptions at Mount St. Helens. Bulletin of Volcanology 57, 356–370.

Giordano, D., Dingwell, D.B., 2003. The kinetic fragility of natural silicate melts. Journal of Physics: Condensed Matter 15, S945–S954.

Gurioli, L., Houghton, B.F., Cashman, K.V., Cioni, R., 2005. Complex changes in eruption dynamics during the 79 AD eruption of Vesuvius. Bulletin of Volcanology 67, 144–159.

Hammer, J.E., Rutherford, M.J., 2002. An experimental study of the kinetics of decompression-induced crystallization in silicic melt. Journal of Geophysical Research 107. doi:10.1029/2001JB000281.

Head, J.W., Wilson, L., 1989. Basaltic pyroclastic eruptions: influence of gas-release patterns and volume fluxes on fountain structure, and the formation of cinder cones, spatter cones, rootless flows, lava ponds and lava flows. Journal of Volcanology and Geothermal Research 37, 261–271.

Herd, R.A., Pinkerton, H., 1997. Bubble coalescence in basaltic lava: its impact on the evolution of bubble populations. Journal of Volcanology and Geothermal Research 75, 137–157.

Heiken, G., Wohletz, K., 1985. Volcanic Ash. University of California Press, Berkley. 246 pp.

Hildreth, W., 1983. The compositionally zoned eruption of 1912 in the Valley of Ten Thousand Smokes, Katmai National Park, Alaska. Journal of Volcanology and Geothermal Research 18, 1–56.

Hort, M., Gardner, J.E., 2000. Constraints on cooling and degassing of pumice during Plinian volcanic eruptions based on model calculations. Journal of Geophysical Research–Solid Earth 105, 25981–26001.

Houghton, B.F., Wilson, C.J.N., 1989. A vesicularity index for pyroclastic deposits. Bulletin of Volcanology 51, 451–462.

Houghton, B.F., Wilson, C.J.N., Smith, I.E.M., 2000. Shallow-seated controls on styles of explosive basaltic volcanism: a case study from New Zealand. Journal of Volcanology and Geothermal Research 91, 97–120.

Houghton, B.F., Wilson, C.J.N., Del Carlo, P., Coltelli, M., Sable, J.E., Carey, R., 2004a. The influence of conduit processes on changes in style of basaltic Plinian eruptions: Tarawera 1886 and Etna 122 BC. Journal of Volcanology and Geothermal Research 137, 1–14.

Houghton, B.F., Wilson, C.J.N., Fierstein, J., Hildreth, W., 2004b. Complex proximal deposition during the Plinian eruptions of 1912 at Novarupta, Alaska. Bulletin of Volcanology 66, 95–133.

Jaupart, C., 1996. Physical models of volcanic eruptions. Chemical Geology 128, 217–227.

Jaupart, C., 1998. Gas loss from magmas through conduit walls during eruption. In: Gilbert, J.S., Sparks, R.S.J. (Eds.), Physics of Explosive Volcanic Eruptions. Geological Society Special Publications, pp. 73–90.

Jaupart, C., Allegre, C.J., 1991. Gas content, eruption rate and instabilities of eruption regime in silicic volcanoes. Earth and Planetary Science Letters 102, 413–429.

Jaupart, C., Vergniolle, S., 1989. The generation and collapse of a foam layer at the roof of a basaltic magma chamber. Journal of Fluid Mechanics 203, 347–380.

Kerswell, R.R., 2005. Recent progress in understanding the transition to turbulence in a pipe. Nonlinearity 18, R17–R44.

Kirkpatrick, R.J., 1981. Kinetics of crystallization of igneous rocks. In: Lasaga, A.C., Kirkpatrick, R.J. (Eds.), Kinetics of Geochemical Processes. Mineralogical Society of America, Washington, DC, pp. 1–81.

Klug, C., Cashman, K.V., 1994. Vesiculation of May 18, 1980, Mount St. Helens magma. Geology 22, 468–472.

Klug, C., Cashman, K.V., 1996. Permeability development in vesiculating magmas: implications for fragmentation. Bulletin of Volcanology 58, 87–100.

Klug, C., Cashman, K.V., Bacon, C.R., 2002. Structure and physical characteristics of pumice from the climactic eruption of Mount Mazama (Crater Lake), Oregon. Bulletin of Volcanology 64, 486–501.

Lautze, N.C., Houghton, B.F., 2005. Physical mingling of magma and complex eruption dynamics in the shallow conduit at Stromboli volcano, Italy. Geology 33, 425–428.

Lejeune, A.-M., Richet, P., 1995. Rheology of crystal-bearing silicate melts: an experimental study at high viscosities. Journal of Geophysical Research 100 (B3), 4215–4229.

Lipman, P.W., Banks, N.G., 1987. Aa flow dynamics, Mauna Loa 1984. U.S. Geological Survey Professional Paper 1350, 1527–1568.

Llewellin, E.W., Mader, H.M., Wilson, S.D.R., 2002. The rheology of a bubbly liquid. Proceedings of the Royal Society of London. A, Mathematical and Physical Sciences 458, 987–1016.

Lofgren, G., 1974. An experimental study of plagioclase crystal morphology: isothermal crystallization. American Journal of Science 274, 243–273.

Lyakhovsky, V., Hurwitz, S., Navon, O., 1996. Bubble growth in rhyolitic melts: experimental and numerical investigation. Bulletin of Volcanology 58, 19–32.

Mangan, M.T., Cashman, K.V., 1996. The structure of basaltic scoria and reticulite and inferences for vesiculation, foam formation, and fragmentation in lava fountains. Journal of Volcanology and Geothermal Research 73, 1–18.

Mangan, M.T., Sisson, T., 2000. Delayed, disequilibrium degassing in rhyolite magma: decompression experiments and implications for explosive volcanism. Earth and Planetary Science Letters 183, 441–455.

Mangan, M.T., Cashman, K.V., Newman, S., 1993. Vesiculation of basaltic magma during eruption. Geology 21, 157–160.

Mangan, M.T., Mastin, L., Sisson, T., 2004. Gas evolution in eruptive conduits: combining insights from high temperature and pressure decompression experiments with steady-state flow modeling. Journal of Volcanology and Geothermal Research 129, 23–36.

Mastin, L.G., Christiansen, R.L., Thornber, C., Lowenstern, J., Beeson, M., 2004. What makes hydromagmatic eruptions violent? Some insights from the Keanakako‘i Ash, Kilauea Volcano, Hawai‘i. Journal of Volcanology and Geothermal Research 137, 15–31.

Means, W.D., Park, Y., 1994. New experimental approach to understanding igneous texture. Geology 22, 323–326.

Métrich, N., Allard, P., Spilliaert, N., Andronico, D., Burton, M., 2004. 2001 flank eruption of the alkali- and volatile-rich primitive basalt responsible for Mount Etna’s evolution in the last three decades. Earth and Planetary Science Letters 228, 1–17.

Munson, B.R., Young, D.F., Okiishi, T.H., 1990. Fundamentals of Fluid Dynamics. John Wiley & Sons, New York. 843 pp.

Navon, O., Lyakhovsky, V., 1998. Vesiculation processes in silicic magmas. In: Gilbert, J.S., Sparks, R.S.J. (Eds.), Physics of Explosive Volcanic Eruptions. Geological Society, London, Special Publications, London, pp. 27-50.

Papale, P., 1998. Volcanic conduit dynamics. In: Freundt, A., Rosi, M. (Eds.), From Magma to Tephra: Modelling Physical Processes of Explosive Volcanic Eruptions. Elsevier, Amsterdam, pp. 55–89.

Papale, P., 1999. Strain-induced magma fragmentation in explosive eruptions. Nature 397, 425–428.

Papale, P., Neri, A., Macedonio, G., 1998. The role of magma composition and water content in explosive eruptions: 1. Conduit ascent dynamics. Journal of Volcanology and Geothermal Research 87, 75–93.

Papale, P., Barsanti, M., Barbato, D., Moretti, R., 2006. A statistical method to determine total H_2O and CO_2 budgets in magmas. Geophysical Research Abstracts 8, 08053, EGU Meeting, Vienna, April 2006.

Parfitt, E.A., 2004. A discussion of the mechanisms of explosive basaltic eruptions. Journal of Volcanology and Geothermal Research 134, 77–107.

Parfitt, E.A., Wilson, L., 1995. Explosive volcanic eruptions: IX. The transition between Hawaiian-style lava fountaining and Strombolian explosive activity. Geophysical Journal International 21, 226–232.

Pinkerton, H., Stevenson, R.J., 1992. Methods of determining the rheological properties of magmas at sub-liquidus temperatures. Journal of Volcanology and Geothermal Research 53, 47–66.

Polacci, M., Pioli, L., Rosi, M., 2003. The Plinian phase of the Campanian Ignimbrite eruption (Phlegrean Fields, Italy): evidence from density measurements and textural characterization of pumice. Bulletin of Volcanology 65, 418–432.

Polacci, M., Corsaro, R.A., Andronico, D., 2006. Coupled textural and compositional characterization of basaltic scoria: insights into the transition from Strombolian to fire fountain activity at Mount Etna, Italy. Geology 34 (3), 201–204.

Pyle, D.M., 1989. The thickness, volume and grainsize of tephra fall deposits. Bulletin of Volcanology 51, 1–15.

Richter, D.H., Eaton, J.P., Murata, K.J., Ault, W.U., Krivoy, H.L., 1970. Chronological Narrative of the 1959–60 Eruption of Kilauea Volcano, Hawaii. U.S. Geological Survey Professional Paper, vol. 537-E. 73 pp.

Rutherford, M.J., Hill, P.M., 1993. Magma ascent rates from amphibole breakdown: an experimental study applied to the 1980–1986 Mount St. Helens eruptions. Journal of Geophysical Research 98, 19667–19685.

Rutherford, M.J., Gardner, J.E., 2000. Rates of magma ascent. In: Houghton, B.F., McNutt, S.R., Rymer, H., Stix, J. (Eds.), Encyclopedia of Volcanoes. Academic Press, San Diego, pp. 207–218.

Saar, M.O.,1998. The relationship between permeability, porosity, and microstructure in vesicular basalts. M.S. Thesis, University of Oregon, 91 pp.

Saar, M.O., Manga, M., 1999. Permeability–porosity relationship in vesicular basalts. Geophysical Research Letters 26, 111–114.

Sahagian, D.L., Proussevitch, A.A., 1998. 3D particle size distributions from 2D observations: stereology for natural applications. Journal of Volcanology and Geothermal Research 84, 173–196.

Self, S., Sparks, R.S.J., 1978. Characteristics of widespread pyroclastic deposits formed by the interaction of silicic magma and water. Bulletin Volcanologique 41, 196–212.

Seyfried, R., Freundt, A., 2000. Experiments on conduit flow and eruption behavior of basaltic volcanic eruptions. Journal of Geophysical Research 105, 23727–23740.

Signorelli, S., Vaggelli, G., Francalanci, L., Rosi, M., 1999. Origin of magmas feeding the Plinian phase of the Campanian Ignimbrite eruption, Phlegrean Fields, Italy: constraints based on matrix-glass and glass-inclusion compositions. Journal of Volcanology and Geothermal Research 91, 199–220.

Simakin, A.G., Armienti, P., Epelbaum, M.B., 1999. Coupled degassing and crystallization: experimental study at continuous pressure drop, with application to volcanic bombs. Bulletin of Volcanology 61, 275–287.

Simkin, T., Siebert, L., 1994. Volcanoes of the World. Geoscience Press, Tucson, AZ.

Sparks, R.S.J., 1978. The dynamics of bubble formation and growth in magmas: a review and analysis. Journal of Volcanology and Geothermal Research 3, 1–37.

Sparks, R.S.J., Brazier, S., 1982. New evidence for degassing processes during explosive eruptions. Nature 295, 218–220.

Sparks, R.S.J., Barclay, J., Jaupart, C., Mader, H.M., Phillips, J.C., 1994. Physical aspects of magma degassing: I. Experimental and theoretical constraints on vesiculation. Volatiles in Magmas. Reviews in Mineralogy, pp. 413–445.

Spilliaert, N., Allard, P., Métrich, N., Sobolev, A.V., 2006. Melt inclusion record of the conditions of ascent, degassing, and extrusion of volatile-rich alkali basalt during the powerful 2002 flank eruption of Mount Etna (Italy). Journal of Geophysical Research 111 (B04203). doi:10.1029/2005JB003934.

Sutton, A.N.,1995. Evolution of a large magmatic system: Taupo volcanic centre, New Zealand. Ph.D. Thesis, The Open University, Milton Keynes, UK, 416 pp.

Swanson, D.A., Duffield, W.A., Jackson, D.B., Peterson, D.W., 1979. Chronological Narrative of the 1969–71 Mauna Ulu Eruption of Kilauea Volcano, Hawaii. U.S. Geological Survey Professional Paper, vol. 1056, pp. 1–55.

Taddeucci, J., Pompilio, M., Scarlato, P., 2005. Conduit processes during the July–August 2001 explosive activity of Mt Etna (Italy): inferences from glass chemistry and crystal size distribution of ash particles. Journal of Volcanology and Geothermal Research 137, 33–54.

Tait, S., Jaupart, C., Thomas, R., Gardner, J., 1998. Constraints on cooling rates and permeabilities of pumice in an explosive eruption jet from color and magnetic mineralogy. Journal of Volcanology and Geothermal Research 86, 79–91.

Toramaru, A., 1989. Vesiculation process and bubble size distributions in ascending magmas with constant velocities. Journal of Geophysical Research 94 (B12), 17523–17542.

Toramaru, A., 1990. Measurement of bubble size distributions in vesiculated rocks with implications for quantitative estimation of eruption processes. Journal of Volcanology and Geothermal Research 43, 71–90.

Toramaru, A., 2006. BND (bubble number density) decompression rate meter for explosive volcanic eruptions. Journal of Volcanology and Geothermal Research 154 (3–4), 303–316.

Vergniolle, S., 1996. Bubble size distribution in magma chambers and dynamics of basaltic eruptions. Earth and Planetary Science Letters 140, 269–279.

Vergniolle, S., Jaupart, C., 1986. Separated two-phase flow and basaltic eruptions. Journal of Geophysical Research 91, 12842–12860.

Vergniolle, S., Mangan, M., 2000. Hawaiian and Strombolian eruptions. In: Houghton, B.F., McNutt, S.R., Rymer, H., Stix, J. (Eds.), Encyclopedia of Volcanoes. Academic Press, San Diego, pp. 447–461.

Walker, G.P.L., 1973. Explosive volcanic eruptions: a new classification scheme. Geologische Rundschau 62, 431–446.

Walker, G.P.L., 1980. The Taupo Pumice: product of the most powerful known (ultraplinian) eruption? Journal of Volcanology and Geothermal Research 8, 69–94.

Walker, G.P.L., 1981. Plinian eruptions and their products. Bulletin Volcanologique 44, 223–240.

Walker, G.P.L., 1989. Spongy pahoehoe in Hawaii: a study of vesicle–distribution patterns in basalt and their significance. Bulletin of Volcanology 51, 199–209.

Walker, G.P.L., Self, S., Wilson, L., 1984. Tarawera 1886, New Zealand – a basaltic Plinian fissure eruption. Journal of Volcanology and Geothermal Research 21, 61–78.

Williams, S.N., 1983. Plinian airfall deposits of basaltic composition. Geology 11, 211–214 (Boulder).

Wilson, L., Head, J.W., 1981. Ascent and emplacement of basaltic magma on the Earth and Moon. Journal of Geophysical Research 86, 2971–3001.

Wilson, L., Parfitt, E.A., Head, J.W., 1995. Explosive volcanic eruptions: VIII. The role of magma recycling in controlling the behaviour of Hawaiian-style lava fountains. Geophysical Journal International 121, 215–225.

Wilson, L., Sparks, R.S.J., Walker, G.P.L., 1980. Explosive volcanic eruptions: IV. The control of magma properties and conduit geometry on eruption column behaviour. Geophysical Journal of the Royal Astronomical Society 63, 117–148.

Zhang, Y., Behrens, H., 2000. H_2O diffusion in rhyolitic melts and glasses. Chemical Geology 169, 243–262.

Zhang, Y., Stolper, E.M., 1991. Water diffusion in basaltic melts. Nature 351, 306–309.